DECLASSIFIED

NACA

$X63-64863$

RESEARCH MEMORANDUM

for the

Bureau of Aeronautics, Department of the Navy

SUMMARY OF FLIGHT DATA OBTAINED

FROM 0.12-SCALE ROCKET-POWERED MODELS OF THE

CHANCE VOUGHT REGULUS II MISSILE

TED NO. NACA AD 398

By Andrew R. Wineman

Langley Aeronautical Laboratory
Langley Field, Va.

NATIONAL ADVISORY COMMITTEE
FOR AERONAUTICS
WASHINGTON
AUG 19 1958

N65-85872

(ACCESSION NUMBER)

74

(PAGES)

(NASA CR OR TMX OR AD NUMBER)

NONE

(THRU)

(CODE)

(CATEGORY)

NATIONAL ADVISORY COMMITTEE FOR AERONAUTICS

DECLASSIFIED

RESEARCH MEMORANDUM

for the

Bureau of Aeronautics, Department of the Navy

SUMMARY OF FLIGHT DATA OBTAINED

FROM 0.12-SCALE ROCKET-POWERED MODELS OF THE

CHANCE VOUGHT REGULUS II MISSILE*

TED NO. NACA AD 398

By Andrew R. Wineman

SUMMARY

The longitudinal static and dynamic stability, the overall duct performance, the drag, and some static and dynamic lateral-stability data were ascertained by flight tests of 0.12-scale models of the Chance Vought Regulus II missile over a Mach number range of 0.8 to 2.1 and a Reynolds number range of 3×10^6 to 12×10^6. Five models were employed: two non-instrumented drag models; two longitudinal-stability models, of which one was the basic configuration and the other was modified with canard trimmers and a low dorsal fairing; and one lateral stability model with a vertical-tail area twice as large as that of the basic configuration.

Adding fixed canard trimmers, deflected 10°, to the basic configuration (1) had negligible effect on the lift and reduced the static stability by about 15 percent at supersonic speeds, (2) increased the damping in pitch about 35 percent, (3) reduced the large negative pitching moment at zero lift at supersonic speeds, (4) improved the performance of the duct from subsonic speeds to a Mach number of 1.6, and (5) increased the minimum drag 6 percent at a Mach number of 2.0 and 42 percent at a Mach number of 0.9. Large, stable values of both the static and dynamic lateral derivatives were obtained from the lateral-stability model by a vector method at a Mach number of 1.8. A qualitative analysis indicated that as a result of a partial fin failure the lateral model rolled at rates above the resonance in yaw sufficient to induce strong cross-coupled motions.

---

*Title, Unclassified.

DECLASSIFIED

INTRODUCTION

At the request of the Bureau of Aeronautics, Department of the Navy, the external aerodynamics and duct performance of the Chance Vought Regulus II (XRSSM-N-9) missile were investigated by the National Advisory Committee for Aeronautics.

The Regulus II is a turbojet-powered, surface-to-surface missile which can be launched from ship or submarine at medium-range targets and cruise at speeds near a Mach number of 2.0. The missile has no horizontal tail and incorporates a nose of high fineness ratio, thin swept wings of low aspect ratio, a highly swept vertical tail, and a scoop inlet with an oblique shock diffuser.

Longitudinal and lateral static stability and control characteristics have been determined from a 0.065-scale model tested in the Langley 4- by 4-foot supersonic pressure tunnel at Mach numbers of 1.41, 1.61, and 2.01. These data are presented in references 1 and 2. Zero-lift drag of the missile was obtained for a Mach number range of 0.8 to 2.2 from flight tests of two rocket-boosted models and reported in reference 3. Wind-tunnel tests were also made at the Lewis Laboratory to investigate the characteristics of several underslung scoop inlets at Mach numbers of 0.66, 1.5, 1.8, and 2.0, and the results are reported in references 4 and 5. The longitudinal and lateral static characteristics of a 0.065-scale model of the modified Regulus II were investigated at Mach numbers of 1.60, 1.80, and 2.0 and reported in reference 6. Longitudinal static and dynamic stability data were obtained from a flight test of a 0.12-scale rocket-powered model for a Mach number range of 0.8 to 2.1 and reported in reference 7. Additional flight-test data have been obtained from two similar rocket-powered models, one a longitudinal-stability model incorporating small canard trimmers, and the other a lateral-stability model with an oversized vertical tail. It is the purpose of this paper to summarize the rocket-model tests of the Regulus II by combining this additional free-flight data with the data published in references 3 and 7. Rocket-boosted models were tested at the Langley Pilotless Aircraft Research Station at Wallops Island, Va.

SYMBOLS

Whenever possible the letter symbols recommended by the American Standard Association in the publication "Letter Symbols for Aeronautical Sciences," ASA Y10.7-1954, were employed.

A	cross-sectional area, sq ft
a	damping constant in yaw used as e^{-at}, 1/sec
b	wing span, ft, or vertical-tail height above model center line, ft
c	chord of airfoil, ft
$\bar{c}$	mean geometric chord, ft
g	acceleration due to gravity, 32.2 ft/sec^2
I_X, I_Y, I_Z	mass moment of inertia in roll, pitch, and yaw, slug-ft^2
I_{XZ}	product of inertia, $\frac{1}{2}(I_Z - I_X)\tan 2\epsilon$, slug-ft^2
$(L/D)_{max}$	maximum lift-drag ratio for zero control deflections
l	length from leading edge of $\bar{c}$, positive rearward, ft
M	Mach number
m	mass of model, slugs
P	period of free oscillation, sec
p,q,r	components of angular velocity about X-, Y-, and Z-axis, respectively, radians/sec
p	pressure; free-stream static pressure when used without a subscript, lb/sq ft
p_t'	pitot stagnation pressure, lb/sq ft
q	dynamic pressure, $\frac{\gamma}{2} pM^2$, lb/sq ft
R	Reynolds number based on $\bar{c}$
S	total wing area, sq ft
t	time, sec
$t_{1/2}$	time required for model oscillations to damp to one-half amplitude, sec

V	velocity, ft/sec
W	model weight, lb
w/w_0	ratio of mass flow of air through the duct to mass flow of air through a free-stream tube of area equal to the inlet capture area A_i
X,Y,Z	orthogonal body axes with the origin at the model center of gravity and the X-axis parallel to the model center line; positive forward, to right when looking forward, and downward, respectively
x,y,z	distances in X, Y, and Z directions
α	angle of attack, deg
β	angle of sideslip, deg
γ	ratio of specific heats of air
$\dot{\gamma}$	rate of change of flight-path angle with time, radians/sec
Δ	increment in a quantity
ϵ	angle between principal axis and X body axis, positive when prinicpal axis is displaced above the X body axis, deg
ζ_θ	fraction of critical damping in pitch of nonrolling model
ζ_ψ	fraction of critical damping in yaw of nonrolling model
θ/L	projected angle between local chord and root chord of a twisted wing for a unit lift load, deg/lb
ϕ,θ,ψ	components of angular displacement from a given attitude about the X-, Y-, Z-axis, respectively
ω	frequency of lateral oscillation, radians/sec
ω_θ	nondimensional undamped natural frequency in pitch of a nonrolling model (ratio of pitching frequency to steady-rolling frequency)
ω_ψ	nondimensional undamped natural frequency in yaw of nonrolling model (ratio of yawing frequency to steady-rolling frequency)

C_D drag coefficient, $\dfrac{\text{Drag}}{qS}$

C_L lift coefficient, $\dfrac{\text{Lift}}{qS}$

C_l rolling-moment coefficient, $\dfrac{\text{Rolling moment}}{qSb}$

C_m pitching-moment coefficient, $\dfrac{\text{Pitching moment}}{qS\bar{c}}$

C_{m_O} pitching-moment coefficient at zero lift

C_n yawing-moment coefficient, $\dfrac{\text{Yawing moment}}{qSb}$

C_Y lateral-force coefficient, $\dfrac{\text{Lateral force}}{qS}$

$C_{Y_\beta} = \dfrac{\partial C_Y}{\partial \beta}$, per radian

$C_{l_\beta} = \dfrac{\partial C_l}{\partial \beta}$, per radian

$C_{l_p} = \dfrac{\partial C_l}{\partial \dfrac{\dot{\phi}b}{2V}}$, per radian

$C_{l_r} = \dfrac{\partial C_l}{\partial \dfrac{rb}{2V}}$, per radian

$C_{L_\alpha} = \dfrac{\partial C_L}{\partial \alpha}$, per degree

$C_{m_\alpha} = \dfrac{\partial C_m}{\partial \alpha}$, per degree

$C_{m_q} = \dfrac{\partial C_m}{\partial \dfrac{\dot{\theta}\bar{c}}{2V}}$, per radian

$$C_{n_{\dot{\alpha}}} = \frac{\partial C_m}{\partial \frac{\dot{\alpha}\bar{c}}{2V}}, \text{ per radian}$$

$$C_{n_\beta} = \frac{\partial C_n}{\partial \beta}, \text{ per radian}$$

$$C_{n_p} = \frac{\partial C_n}{\partial \frac{\dot{\phi}b}{2V}}, \text{ per radian}$$

$$C_{n_r} = \frac{\partial C_n}{\partial \frac{rb}{2V}}, \text{ per radian}$$

$$C_{n_{\dot{\beta}}} = \frac{\partial C_n}{\partial \frac{\dot{\beta}b}{2V}}, \text{ per radian}$$

$C_{L_{\alpha_r}}$ lift-curve slope for rigid wing

$C_{L_{\alpha_e}}$ lift-curve slope for elastic wing

A dot over a quantity indicates first derivative with respect to time; a double dot indicates second derivative with respect to time.

Ratios of the amplitudes of envelopes of oscillations are expressed by $\left|\frac{C_Y}{\beta}\right|$, $\left|\frac{\dot{\phi}}{\beta}\right|$, etc.

Subscripts:

ac   aerodynamic center

cg   center of gravity

d   duct

e   exit

i   internal or inlet

b   base

max   maximum

min   minimum

s   standard sea-level conditions $\left(p_s = 2,116 \text{ lb/sq ft}\right)$

t   total

trim   trim conditions $\left(C_m = 0\right)$

DESCRIPTION OF MODELS

Five 0.12-scale models of the Regulus II missile, constructed by Chance Vought, were used in the flight-test program; two for longitudinal stability, one for lateral stability, and two for zero-lift drag. The geometry of each model is shown by sketches in figure 1. Model coordinates and the duct area distribution are listed in tables I, II, and III. The weights, center-of-gravity locations, and moments of inertia are listed in table IV. Photographs of the models and of the launcher are shown in figure 2.

The fuselage was basically a body of revolution with a moderate boattail and a nose fineness ratio of 4.50. It was built in three sections of laminated mahogany and aluminum castings. The wings and canard trimmers were of steel and the fins were of aluminum; all were finished within a few thousandths of an inch to the coordinates given in table III. The scoop-type inlet was built from an aluminum casting but most of the duct and boundary-layer bleeds were molded from fiber glass. The base area of the model was proportionally larger than that of the missile to insure sonic velocities near the duct exit. The ratio of base annular area to total wing area was 0.0237. A sketch of the longitudinal cross section of the duct is shown in figure 1(e).

Model 1

Model 1, shown in figures 1(a) and 2(a), was disturbed in pitch by seven pulse rockets with a thrust impulse of 20 pound-seconds each. A ventral fin, of the same airfoil section and plan form as the vertical tail, was added to suppress cross-coupled motions between the pitch and yaw planes by increasing the lateral stability of the model.

DECLASSIFIED

Model 2

Model 2 was used to determine longitudinal stability of a later version of the Regulus II configuration. A sketch of this model is shown in figure 1(b) and a photograph in 2(b), and details of the small canard trimmers are shown in figure 1(e). The canard trimmers were fixed at a deflection of 10°, this area was about 2 percent of the exposed wing area, and this span was slightly less than the maximum body diameter. Except for a control housing and canard trimmers, model 2 and model 1 were geometrically similar. Coordinates of these modifications are listed in tables II and III.

Model 3

A three-view sketch of model 3 is shown in figure 1(c), a photograph of the model in figure 2(c), and a photograph of the model-booster combination in figure 2(d). Since this model was used to investigate lateral stability of the Regulus II configuration, pulse rockets were located to disturb the model in yaw; six were mounted in the nose of the model. An oversized vertical tail was employed in lieu of a ventral fin; otherwise model 3 was similar to model 1. The vertical tail was designed large enough to furnish the same static directional stability as the full-scale missile-autopilot system. During manufacture, a section on the right side of the vertical tail was inadvertently undercut; it was then filled with a hard plastic. The affected area is visible in figure 2(d). The maximum depth of the filled undercut was estimated to be 1/4 of the local thickness of the fin. This filling came out in flight, probably because of the flexibility of the fin.

Models 4 and 5

Models 4 and 5 were as nearly identical as possible and were both used to determine total drag. A sketch of models 4 and 5 is shown in figure 1(d). These models did not have ventral fins but were geometrically similar in other respects to model 1. The drag models were tested with a forward center-of-gravity location to insure sufficient static stability for a nearly zero-lift flight path. Neither model contained any instrumentation but each had a smokepot to aid the radar operators in tracking the model as the booster separated.

INSTRUMENTATION

Models 1, 2, and 3 were equipped with a standard NACA telemeter to transmit ten continuous measurements to the ground during flight.

Models 4 and 5 contained no telemeter equipment. All models were tracked by two ground radar units; a modified SCR-584 to determine the position of the model in space, and a CW Doppler unit to measure its line-of-sight velocity. Ambient pressure, temperature, dew point, and velocity of winds aloft were measured by a rawinsonde balloon launched immediately after each model flight.

Models 1, 2, and 3 were instrumented to measure angle of attack, angle of yaw, normal acceleration, transverse acceleration, longitudinal acceleration, pitot stagnation pressure, duct total pressure, duct static pressure, base pressure, and an angular acceleration. The angular acceleration in pitch was measured for models 1 and 2, but the angular accelerometer in model 3 was used to determine roll acceleration. An average roll rate was obtained by measuring the angular rate of the polarized telemeter signal received from the model.

Total pressure in the duct was measured by a slotted integrating total-pressure rake. The duct static pressures was measured by four manifolded static-pressure holes located around the periphery of the duct at the measuring station. The location of these pickups in the duct is shown in figure 1(e). The location of the holes in the annulus of the base, manifolded to measure an average base pressure, is also shown in figure 1(e). The duct static pressure of models 1 and 3 was measured directly. The duct total pressure was determined from the measured difference between the duct static and the duct total pressure. The accuracy of the duct measurements of model 2 was improved by using low-range gages to measure the difference between the free-stream pitot pressure and the duct static pressure and also between the free-stream pitot pressure and the duct total pressure. Additional accuracy of the pressure measurements was obtained for model 2 by eliminating the base pressure pickup and using this telemeter channel for a low-range pressure cell on the free-stream pitot pressure pickup in conjunction with the existing high-range pressure cell.

TESTS AND ANALYSIS

Tests

Models 1, 2, 3, and 5 were all boosted to supersonic speeds by a pair of solid-propellant Deacon rocket motors. The booster, shown in figure 2(d), was typical of all models except model 4, which was boosted by a single Deacon unit. Each motor supplied about 6,000 pounds of thrust for 3 seconds. When the booster motors exhausted their fuel, the booster separated from the model by vitue of its higher deceleration along the flight path. Pulse rockets, igniting in a predetermined sequence, disturbed the model from its trim condition as it coasted to

higher altitudes and decreased in speed. The static and dynamic stability parameters were obtained from transient forces measured during the time the model oscillated freely about the trim angle of attack or angle of sideslip.

Flight conditions of each model throughout the test Mach number range are shown in figure 3: the ratio of ambient static pressure to sea-level standard pressure in figure 3(a), the Reynolds number based on the mean geometric chord of the wing in figure 3(b), and the Mach number range corresponding to each pulse rocket and separation disturbance in figure 3(c).

The right wing, the vertical tail, and the ventral fin of each model were statically loaded at various spanwise stations along the quarter-chord and half-chord lines. Dial gages located at the leading and trailing edges of the wing, or fin, were used to measure the twist and the displacement of the local chord with respect to the root chord at four or five stations along the span. The structural influence coefficients θ/L (twist per unit bending load) of each lifting surface were determined from these static tests and are presented in figure 4.

Reduction of Data

Aeroelasticity.- The aeroelastic properties of the wing were calculated for the test Mach number range by the method of reference 8. The ratio of the lift-curve slopes for rigid and elastic wings and the forward shift of the aerodynamic-center location resulting from wing flexibility were calculated and are shown in figure 5. These calculations required the measured twist of the wing for a unit bending load (fig. 4(a)) and the theoretical span-load distribution obtained for various Mach numbers from references 9 and 10.

The ratio of rigid to elastic lift-curve slopes and the shift of the aerodynamic center were not calculated for the vertical fins. The longitudinal models had sufficient directional stability for the elastic condition and data from the lateral model were qualitative since part of the vertical tail was lost in flight. However, the influence coefficients of the vertical fins are included in figure 4 for general information.

Longitudinal stability.- Static and dynamic stability parameters, calculated by methods described in reference 11, were obtained from the short-period pitch oscillations of the model after the disturbances that occurred at the Mach numbers shown in figure 3(c). All angles, forces, and moments measured in flight were referred to the center of gravity of the model. Forces, moments, and duct pressures were converted to nondimensional form, and results similar to the samples shown in

figure 6 were obtained for each oscillation. The period and the loga-
rithmic decay of the measured transient forces were used in a two-
degree-of-freedom analysis to determine average values of C_{m_α} and
$C_{m_q} + C_{m_{\dot\alpha}}$ for the range of angle of attack obtained in flight. The
total pitching moment, without the damping moments, was obtained from
the measured pitching acceleration $\dot q$ by the following relation:

$$C_m = \frac{I_Y \dot q}{qS\bar c} - \left(C_{m_q} + C_{m_{\dot\alpha}}\right)\frac{\bar c}{2V} q + C_{m_{\dot\alpha}} \frac{\bar c}{2V} \dot\gamma \tag{1}$$

The last term was negligible and was eliminated from the calculation;
the pitching velocity q, used in the equation to account for the damping
moments, was obtained indirectly from measured values of α and normal
acceleration. Sample variations of C_m and C_L are presented in
figure 6(b).

Duct.- The total-pressure recovery of the duct, or the ratio of the
average duct total pressure to the free-stream total pressure, was deter-
mined by measuring pressure differences as described in the section
entitled "Instrumentation" and by applying the adiabatic ratio of the
free-stream total pressure to measured pitot stagnation pressure. Once
the static pressure in the duct was determined, the mass-flow ratio
could be calculated by the following relation:

$$\frac{w}{w_0} = \frac{p_d A_d M_d}{p A_i M} \left(\frac{1 + \frac{\gamma - 1}{2} M_d^2}{1 + \frac{\gamma - 1}{2} M^2}\right)^{1/2} \tag{2}$$

The Mach number in the duct was determined from the measured static and
total pressures. The reference inlet area ($A_i = 6.68$ square inches)
was the cross-sectional area of the duct projected to a plane perpendicu-
lar to the model center line at the inlet lip, station 36.54. At sub-
sonic speeds the cross-sectional area at the measuring station was A_d
in equation (2). However, when the duct exit was certain to be sonic, at
flight Mach numbers greater than $M = 1.1$, it was found that w/w_0 could
be obtained more accurately by assuming that a normal shock, $M_d = 1.0$,
existed near the duct exit. The static pressure near the duct exit was
obtained from the measured duct total pressure and adiabatic channel
relations, assuming a 1-percent loss in total pressure between the meas-
uring station and the minimum station. Since all pressure measurements
were continuous, the variations of the total-pressure recovery $p_{t,d}/p_t$

and mass-flow ratio w/w_0 with angle of attack were obtained. Sample plots, chosen to show greatest variations, are shown in figures 6(c) and 6(d).

Drag.- Total drag coefficients were obtained from accelerometer data for models 1 and 2 and checked with data from CW Doppler radar after corrections for wind and flight-path angle were made. Drag data of models 4 and 5 were determined from radar data alone. Sample variations of the total drag of models 1 and 2 are shown in figure 6(e). Total drag includes internal drag of the duct, any spillage drag caused by the overflow of air at the inlet, and base drag. The internal drag and base drag of the model are subtracted from the total drag, since the internal duct rearward of the diffuser and the base annulus area are not the same as in the prototype. The remaining drag, which includes any spillage or additive drag, is referred to as external drag.

The internal drag is determined from the momentum loss between the entrance and exit of the duct while the model is at the angle of attack for minimum drag. Once the mass-flow ratio, the exit Mach number, and the exit pressure of the duct are known it is possible to calculate the internal drag coefficient by the following relation:

$$C_{D,i} = \frac{2A_e}{S}\left[\frac{w}{w_0}\frac{A_i}{A_e} - \frac{p_e}{p}\left(\frac{M_e}{M}\right)^2 - \frac{p_e - p}{\gamma p M^2}\right] \tag{3}$$

As in the case of the mass-flow ratio, the static pressure at the exit was obtained from the measured duct total pressure and transferred to the exit by means of the appropriate area ratios, assuming a 1-percent loss in total pressure resulting from friction over the distance from the measuring station to the exit station. Knowing the Mach number at the exit, the static pressure at the exit may be obtained from adiabatic gas relations. The internal drag may be determined for the condition in which the exit of the duct is not choked ($M_d < 1.0$ at minimum-area station near exit) by assuming that the exit static pressure is equal to the base pressure measured on the annulus. Since the base pressure was not measured on model 2, the exit pressure at subsonic speeds was determined from the pressure coefficient of the base annulus of model 1. These average, nondimensional pressure coefficients of the base were converted to base drag coefficients and used with the internal drag coefficients to obtain the external drag of model 2 from the total measured values.

By assuming the drag polars to be parabolic (this was permissible since C_D varied linearly with C_L^2 over the angle-of-attack range of the investigation), it was possible to calculate $(L/D)_{max}$ of the model

and the lift coefficient for $(L/D)_{max}$ (designated C_L'') by the following relations:

$$C_L'' = \sqrt{(C_L')^2 + \frac{C_{D_{min}}}{dC_D/dC_L{}^2}} - C_L' \qquad (4)$$

$$(L/D)_{max} = \frac{1}{2 \dfrac{dC_D}{dC_L{}^2} C_L''} \qquad (5)$$

where the minimum drag coefficient $C_{D_{min}}$, the lift at $C_{D_{min}}$ (designated C_L'), and the drag due to lift $dC_D/dC_L{}^2$ were known. It should be remembered that the value of $(L/D)_{max}$ calculated by this method is dependent upon the origin of the inputs into the equations.

Lateral stability.- Average values of C_{Y_β}, C_{l_r}, C_{l_β}, $C_{n_r} - C_{n_{\dot\beta}}$, and C_{n_β} were determined for model 3 at $M = 1.8$ by a vector-analysis method developed in reference 12. These coefficients were calculated by using vector solutions of the equations of motion describing the side force, rolling moment, and yawing moment of the model and the essential features of the oscillatory, or Dutch roll, part of the lateral response of pulse-rocket disturbances in the yaw plane. The characteristics of the oscillation used to solve for the magnitude and direction of the unknown vectors were: the period, the damping factor, the slope of the lateral-force coefficient, the phase angle (or time lag between the angle of sideslip and the lateral force and also between the angle of sideslip and the angular acceleration in roll), and the ratio of the maximum amplitudes of the sideslip transient to the maximum amplitudes of the transients of lateral force and rolling acceleration. Vectors representing the time derivatives and integrals of measured displacements, velocities, and accelerations were obtained directly as functions of the rotating frequency of the vector and the damping of the transient. The weight vector was assumed to be negligible, the slope C_{Y_β} was obtained directly from the cross plots, the angle of attack in radians was an average value for the duration of the oscillation, and the roll rate was the integral of the measured roll acceleration.

Only the data resulting from the first pulse rocket could be ana-
lyzed by the method of reference 12 since the rolling velocity of
model 3 reached high rates and the lateral mode of the motion coupled
with the longitudinal mode. The divergence boundaries of model 3 were
calculated by the method of reference 13, using the measured values of
the pitch parameters of model 1 and estimating the lateral parameters
of model 3 with the help of reference 1 and some unpublished wind-
tunnel data.

Accuracy.- The accuracy of a set of data is often difficult to
determine since it involves not only an estimation of the precision of
the measured quantities but also an estimation of the systematic and
accidental errors encountered in reducing the data to final form. The
reliability of data is often substantiated by comparison of results
obtained by using different testing techniques, or by the repeatability
of results obtained by using the same technique. Experience has shown
that, when such comparisons can be made, the magnitude of the accuracy
is indicated by deviations of the results. However, a theoretical
accuracy can be calculated by several methods, such as mean-square error,
probable error, or average error. The accuracy of the data used herein
was calculated by the method of probable error as described in refer-
ence 14. The method is outlined in the appendix and the results for
models 1, 2, and 3 are shown in table V.

RESULTS AND DISCUSSION

Lift

Sample plots of the lift coefficient as a function of angle of
attack for models 1 and 2 are presented for three representative Mach
numbers in figure 6(a) to indicate the range and linearity of these
variables. Over the largest range of angle of attack, about 20° at
$M = 0.9$, the lift curve varied less than 3 percent from a straight line.

The lift-curve slopes of model 1 and model 2 and slopes obtained
from the wind-tunnel data of reference 1 are presented in figure 7.
These data for models 1 and 2 were obtained from measured cross plots
similar to those shown in figure 6(a) and represent the elastic loads
of the models; however, the lift-curve slopes obtained from reference 1
were essentially rigid-wing data. The ratio of rigid to elastic C_{L_α}
of the flight model was shown in figure 5(a). The lift-curve slope
decreased from about 0.065 at $M = 1.0$ to 0.041 at $M = 2.0$. It can
be concluded that there was good correlation between the lift data for
the two flight tests and the wind-tunnel test at supersonic speeds. It
can also be seen from figure 7 that the effect of the canard trimmers

on the lift-curve slope was small, except possibly at low transonic speeds. It was difficult to determine any flow mechanism that would produce a loss in the lift-curve slope at these speeds but the difference in the overall configurations of models 1 and 2 was evidently sufficient to produce this change in C_{L_α}.

Static Stability

The static longitudinal stability of models 1 and 2 is shown in figure 8. The period of the measured pitch oscillations is shown in figure 8(a), the nondimensional spring constant of the airframe in figure 8(b), and the location of the aerodynamic center in figure 8(c). The longitudinal location of the center of gravity relative to the wing was the same for both models, forward of the leading edge of the mean geometric chord by 45.2 percent of the mean geometric chord. With the ventral fin, the lateral stability was sufficient at supersonic speeds to limit the angle of sideslip to less than $\frac{1}{2}^\circ$ and the roll rate to less than 1 radian per second. At transonic and subsonic speeds the maximum angle of sideslip was less than $1\frac{1}{2}^\circ$ and the roll rate was less than 2 radians per second.

The period shown in figure 8(a) was obtained from transients where the pitching moment varied linearly with the lift. Both the period and C_{m_α} indicated that model 2 was more stable than model 1 at transonic speeds but slightly less stable than model 1 at supersonic speeds. Thus, when small fixed canard trimmers and a dorsal fairing were added to the basic configuration, C_{m_α} increased negatively by as much as 46 percent at $M = 1.0$ and decreased about 15 percent at supersonic speeds. Since the prototype will be flown at a static margin near zero for larger response, the loss in C_{m_α} resulting from the canards is not critical at supersonic speeds, and it is desirable from an automatic-control standpoint to have a smooth variation of C_{m_α} throughout the speed range of the missile. It would be easier to match the characteristics of the autopilot to the airframe aerodynamics if C_{m_α} varied through the transonic region as for model 2 than if it varied as for model 1.

The location of the aerodynamic center with respect to the leading edge of the mean geometric chord is shown in figure 8(c). At supersonic speeds the aerodynamic-center locations of both models 1 and 2 were fairly constant, that of model 1 at $0.35\bar{c}$ and that of model 2 at $0.25\bar{c}$. The tunnel tests indicated that for a rigid wing the aerodynamic center would be about $0.07\bar{c}$ forward of the flight-test values. At $M = 0.9$

the aerodynamic center of model 1 was at about $0.10\bar{c}$ and for model 2 it was at about $0.05\bar{c}$. The variation of the aerodynamic-center location with Mach number was improved throughout the transonic region when canard trimmers and a body fairing were added to the basic configuration.

Dynamic Stability

The longitudinal dynamic stability of models 1 and 2 is demonstrated in figure 9. The time required for the maximum amplitude of the pitching transients to reduce to one-half of a given value, for the particular flight conditions of models 1 and 2, is shown in figure 9(a). To give a nondimensional value of the damping in pitch, the rotatory damping derivative $C_{m_q} + C_{m_{\dot{\alpha}}}$ is presented in figure 9(b).

When $C_{m_q} + C_{m_{\dot{\alpha}}}$ was compared with the damping-in-pitch data of some twenty configurations of reference 15, it was apparent that models 1 and 2 generally had better damping in pitch than the tailless configurations, and damping comparable to that of most configurations that had a horizontal tail or used canard surfaces. The damping data of figure 9(b) followed the trend associated with wings incorporating low angles of sweepback - that is, a lower value of damping at transonic speeds than at the low supersonic Mach numbers. However, as shown in this figure, both models 1 and 2 were dynamically stable throughout the range from $M = 0.8$ to $M = 2.0$. The variation of the damping in pitch with Mach number is often more important than the absolute magnitude for a missile requiring an automatic control system. The damping-in-pitch derivative of model 1 varied from -6 to -14, and that of model 2 varied from -8 to -19.

When the airframe damping is small compared with that required of a missile in a controlled maneuver, as it is in this case, these variations lose their significance since a large percentage of the required damping is added artificially. On an average the damping of model 1 was about 5 percent of its critical damping and that of model 2 about 6 percent of critical, but the total damping required for the tactical missile may be as much as 50 percent of critical.

Trim

The trim angle of attack, the trim lift coefficient, and the pitching-moment coefficient at zero lift are shown in figure 10 for the test Mach number range of models 1 and 2. These were the angle of attack and lift measured when the total pitching moment, corrected for the damping moment was zero. These trim values correspond to the steady-state part of the transients of α and C_L. All data were measured for

the center of gravity located at $0.45\bar{c}$ ahead of the leading edge of $\bar{c}$. (See figs. 1(a) and 1(b).)

The trim lift coefficient of model 1 was relatively large at supersonic speeds. (See fig. 10.) When the center of gravity was located at the leading edge of the mean geometric chord, as in reference 1, excessive negative elevon deflection would be required to maintain trimmed level flight at altitude and the extra drag associated with these elevon deflections would reduce the effective range of the missile. To combat these difficulties two sizes of small canard trimmers were located well forward on the nose and tested in the 4- by 4-foot supersonic pressure tunnel at $M = 2.01$ (ref. 2). It is quite apparent from figure 10 that the small canard trimmers of model 2 (fixed at a deflection of 10°) were effective in changing the trim to a more favorable value. For the particular stability of the flight model, the canards increased the trim angle of attack about $1\frac{1}{2}^{\circ}$ throughout the Mach number range. Reference 2 indicates that the control housing was slightly detrimental to the trim lift at $M = 2.0$, although it had a negligible effect on the total lift and drag of the airframe. It was possible that the control housing may have been responsible for the slight irregularities noted in the trim characteristics of model 2 at supersonic speeds.

The pitching moment at zero lift C_{m_O} is a function only of the aerodynamic shape of a configuration and is not dependent upon the longitudinal location of the center of gravity. The amount of control deflection required to pitch a missile to a predetermined trim is largely dependent upon the value of C_{m_O}. Since cruise missiles fly at constant altitudes it is often desirable to have a configuration for which the aerodynamic flow produces a positive C_{m_O} of sufficient magnitude to obtain the cruise lift coefficient without deflection of the controls.

Aside from some variations at transonic speeds, C_{m_O} for both models 1 and 2 was regular with Mach number and nearly constant above $M = 1.6$. However, because of the underslung inlet and duct, C_{m_O} for the basic configuration was negative at all Mach numbers. (See curve for model 1 in fig. 10.) About 12° of elevon deflection would be required to offset C_{m_O} before any elevon power could be used to obtain a positive trim lift. With the small canard trimmers, only about 2° of elevon deflection would be required to obtain positive lift at supersonic speeds; however, C_{m_O} in the transonic regime is not improved. In conclusion, the negative value of C_{m_O} for model 1 was

too large for efficient cruise at supersonic speeds, and adding the canard trimmers reduced C_{m_O} to nearly zero at supersonic speeds but increased it at low transonic speeds.

Duct

The inlet of models 1 and 2 operated satisfactorily throughout the test Mach number range of 0.8 to 2.1; however, the duct data of model 3 were obviously erroneous at Mach numbers less than 1.8, and therefore are presented only for $M = 1.8$ to $M = 2.0$. The total-pressure recovery and the mass-flow ratio, averaged across the duct at its largest cross section, were used to indicate the performance of the duct and are shown in figure 11. The influence of angle of attack on the pressure recovery and the ratio of the mass flows, at three representative Mach numbers, is shown in figures 6(c) and 6(d), respectively.

Since the scoop inlet was designed for cruise near $M = 2.0$, a supersonic diffuser was utilized in lieu of a normal-shock diffuser to reduce inlet spillage and to increase the pressure recovery. The amount of total free-stream pressure that can be recovered by the inlet-diffuser-duct system is dependent upon the losses in that system. These include shock losses, losses due to slip regions in the diffuser behind intersecting shock waves, and losses due to turbulence in the subsonic part of the duct. When the kinetic energy of a flow is transformed into potential energy by means of a supersonic diffuser, a different flow pattern will exist at the inlet for almost every combination of back pressure and Mach number. Shock patterns believed to have formed on the inlet of the flight model as it decelerated through the speed range are shown in sketches in figure 11(b). An excellent treatise on the flow mechanism of this type of duct can be found in the analysis section of reference 16.

Consider the four Mach number regions indicated by the sketches in figure 11 and note the changes in the nature of the pressure recovery and the mass-flow ratio at $M = 1.4$, 1.6, 1.8, and 2.0. It was believed that the character of the flow in and around the inlet significantly changed near these Mach numbers. Since the supersonic flow was started through the diffuser at the maximum Mach number, which was obtained when the model separated from the booster rocket, the flow will be discussed for regions of decreasing Mach number - first from the maximum to $M = 1.8$. For this entire region the flow was believed to be supercritical, becoming more nearly critical as the speed decreased to $M = 1.8$. This was substantiated by the pressure recovery and mass-flow ratio for critical flow as determined by the wind-tunnel tests of reference 5, which are included in figure 11 for comparison. Normal-shock recovery and the theoretical maximum recovery of the duct (an inclined

shock plus a normal shock within the duct) were also calculated to
establish a reference for the flight-test data. In this supercritical
flow regime the oblique shock, emanating from the wedge of the lower
lip of the inlet, covers the entire inlet face and prevents any of the
flow from spilling outward from behind the shock. As the Mach number
(or the free-stream stagnation pressure) decreases, the transition
shocks moved upstream closer to the diffuser minimum and yielded a more
efficient system, as evidenced in figure 11(a) by the relative increase
in pressure recovery between M = 2.0 and M = 1.8. The fact that the
mass-flow ratio appears to be greater than 1 at M = 1.95 is attributed
to the fact that the arbitrarily chosen capture area, used to nondimen-
sionalize the mass flow, probably did not correspond exactly with the
local flow that existed on the flight model at that particular Mach num-
ber. The actual mass flow through the inlet was the important parame-
ter. Critical flow, a condition in which a high recovery and a large
mass flow occur at the same time, was believed to exist at M = 1.9.
With respect to the normal-shock and the two-shock recoveries the pres-
sure recovery of the duct was a maximum and the mass-flow ratio was
near unity. From figure 11 it can be seen that at M = 1.9 the mass-
flow ratio was unity and the measured pressure recovery was 86 percent
of the free-stream total pressure while the normal-shock recovery was
77 percent of the total pressure. The good agreement with the tunnel
data of reference 5 also indicates that the flow in the flight model
was nearly critical, particularly at M = 1.8. As the flight model
decelerated to lower Mach numbers the oblique shock on the inlet
steepened and air probably spilled outward from the inlet as the shock
lifted from the inlet face. As long as the shock reflected from the
boundary-layer splitter plate, this spilled air would decrease the
mass-flow ratio in the duct without any relative reduction of pressure
recovery. This was evidenced as the models slowed down from M = 1.95
to M = 1.80.

     As model 1 decelerated through M = 1.8 (a slightly lower Mach
number for model 2) the inclined shock was no longer reflected from the
boundary-layer splitter plate on the roof of the inlet but formed a
normal leg forward of the splitter plate. This appreciably increased
the area available for spillage, and the mass flow of air entering the
duct was reduced abruptly, as indicated in figure 11(b). The pressure
recovery was also reduced relative to the normal-shock and two-shock
systems, indicating additional losses within the duct, probably as a
result of the slip planes originating from the intersecting shocks at
the inlet. As the Mach number became lower the shock continued to
approach more closely a normal-shock pattern over the inlet, the mass
flow became subcritical, and additional losses were encountered in the
duct since the pressure recovery came nearer to normal-shock recovery.
Since the measured pressure recovery was equal to the theoretical
recovery of a normal shock between M = 1.4 and M = 1.5, and since
the measured data included losses other than losses through a normal

shock, it is reasonable to assume that the normal shock covered the
entire duct at a Mach number near M = 1.4. It should be noted that
for Mach numbers greater than M = 1.6 data from models 1 and 2 agreed
well within the accuracy of these tests, but for Mach numbers less than
M = 1.6 data from the two models differed by nearly a constant amount.
The geometrical difference between model 1 and model 2 was the canard
trimmers.

    The general effect of the canard trimmers was to increase the per-
formance of the duct at all Mach numbers below M = 1.6, as evidenced
by the data in figure 11. It was shown from the tunnel tests of refer-
ence 5 that if the model was at an angle of attack of 0°, the angle of
attack of the flow just forward of the inlet was about 1^O. Thus it was
reasonable to assume that there was a cross flow on the inlet ramp of
model 1, and in all probability the interaction of the downwash from
the canard trimmers of model 2 would reduce the magnitude of this cross-
flow sufficiently to increase the mass flow of the duct. It was noted
that at the design condition, M = 2.0, where an oblique shock was
across the entire face of the inlet, the pressure recoveries of model 1
and model 2 were nearly identical, indicating little or no difference
in spillage.

    The duct data for model 3 agreed nearly exactly with the measured
data for models 1 and 2 over the Mach number range of 1.80 to 2.05, but
as the model decelerated from M = 1.8 a large and definite discon-
tinuity in the data suggested that the duct had become damaged. Although
no concrete cause for this relative increase in the measured mass flow
and pressure recovery could be established, it was suspected that loads
exerted by the oversized vertical tail below M = 1.8 distorted the
duct sufficiently to change the minimum area near the exit.

    The performance of the duct was also sensitive to changes in
angles of attack, as shown by the data in figures 6(c) and 6(d). The
variation of the pressure recovery and mass-flow ratio seemed to fall
naturally into three categories, each dominated by a particular flow
pattern over the inlet: first, near the design Mach number where an
inclined shock was over most of the inlet; second, for Mach numbers
between 1.4 and 1.7 where the shock was a combination of an inclined
and a normal shock; and third, for Mach numbers less than M = 1.4
where a normal shock is detached from the inlet lip. Although the data
of model 1 showed some variation with angle of attack near the design
Mach number, both models 1 and 2 demonstrated the largest change between
M = 1.45 and M = 1.61 at negative angles of attack. Both the pres-
sure recovery and mass-flow ratio increased approximately $1\frac{1}{2}$ percent of
the value at $\alpha = 0^O$ for each degree of increase in angle of attack.
In general the duct data for model 2 was less sensitive to change in
angle of attack than the data for model 1. Except for the region

between $M = 1.4$ and $M = 1.6$, the data from model 2 could be considered constant with angle of attack.

The flow in the duct of each flight model was considered stable over the test ranges of Mach number and angle of attack. Between $M = 1.5$ and the maximum, the measured pressures of models 1, 2, and 3 fluctuated by as much as $4\frac{1}{2}$ percent of the free-stream total pressure; however, most variations were less than 1 percent. If the variation is less than 5 percent, the duct is considered to have a stable flow condition. The largest variations were random in nature and occurred at the peak Mach numbers of models 1 and 2. The duct of model 3 pulsated at a steady frequency corresponding to the natural bending frequency of the oversized vertical tail but the amplitude was never greater than 2 percent. The flow in the duct of model 1 was disturbed abruptly at $M = 2$ when one of the pulse rockets discharged just forward of the inlet. Although a sharp pressure jump was measured within the duct, the flow was reestablished in a steady-state condition within 0.02 second, indicating a relatively stable flow.

Drag

The measured minimum-drag coefficients of models 1, 2, 4, and 5; the measured base drag coefficient of model 1; the calculated internal drag coefficient of the duct; and the minimum external drag coefficients of models 1 and 2 are all presented in figure 12. The drag due to lift, the lift coefficient for minimum drag, the maximum lift-drag ratio, and the lift coefficient for $(L/D)_{max}$ are presented in figure 13. These data were determined from curves of drag coefficient plotted against lift coefficient similar to the samples shown in figure 6(e). It should be remembered that all controls were fixed, the canard trimmers at 10° and the elevons at 0°. However, it is believed that the variation of the total drag with Mach number, shown in figure 12(a), is a good indication of the variation of the trim data with Mach number. Measured results from four independent flight tests of nearly identical configurations of the Regulus II are shown in this figure.

The minimum-drag coefficient of model 1 nearly coincides with the zero-lift data of model 4 from $M = 0.8$ to $M = 1.5$. From $M = 1.5$ to $M = 2.1$ the data for model 1 agrees favorably with that for model 5. However, from $M = 1.50$ to $M = 1.75$ the minimum-drag coefficient of model 4 disagrees with the data of models 1 and 5 by an amount greater than the estimated probable accuracy of the measured data. As explained previously, the shock patterns at the inlet for this range of Mach number were quite variable and there probably existed some inconsistencies of the local boundary conditions between the flights. This difference

in drag could be caused by a reduction in spillage due to different conditions at the inlet.

Canard trimmers and the fairing that simulated a control housing were the only differences between models 1 and 2 (see fig. 1); however, the minimum drag of model 2 was larger than anticipated over most of the Mach number range. Figure 12 indicates that the minimum-drag coefficient for model 2 was only slightly larger than that for model 1 near M = 2.0 but nearly 50 percent larger at subsonic speeds. It can be seen from the estimated probable errors in table V that the minimum-drag coefficient for model 2 was as reliable as that for model 1. It is possible that unfavorable interference caused by the canard trimmers and fairing could produce the increase in minimum drag noted between models 1 and 2 at the lower Mach numbers, but unfortunately no comparisons from tunnel tests or flight tests were available for these speeds. At lower Mach numbers this coefficient was considered high for the model with the canard trimmers and fairing, although there was nothing from the flight test to suggest that the errors were greater for this model than for the flight models which showed good agreement. Fortunately, during the part of the flight of model 2 for which the test data were determined (M = 0.8 to M = 2.0), the Mach number was measured by two independent techniques and these data agreed with each other within one-half of 1 percent at supersonic speeds and $1\frac{1}{2}$ percent at subsonic speeds. Data from the longitudinal accelerometer was integrated along the flight path to obtain velocity, and these values agreed within 1 percent with the velocity obtained from ground-based CW Doppler radar. Although it was believed that the drag of model 2 was vindicated, an explanation of the relatively large difference between the minimum drag coefficients of model 1 and model 2 would be pure conjecture.

The internal drag of model 2, calculated from the total momentum loss in the duct, agreed almost exactly with that of model 1. Although the base pressure was measured only on model 1, the base pressure coefficient of model 2 was assumed to have the same variation with Mach number. In these tests the variation of base drag and internal drag was never greater than 1 percent and $2\frac{1}{2}$ percent, respectively, of the minimum external drag.

The external drag coefficient, shown in figure 12(c), was obtained from the measured minimum drag coefficient corrected for the internal and base drag coefficients. No estimates were made for the additive drag associated with the spillage of air from around the scoop inlet, since this was considered part of the external drag and was therefore not excluded from the measured data. The external drag coefficient of model 1 varied from 0.024 at subsonic speeds to 0.045 at M = 1.3 and reduced to 0.033 at M = 2.1. The values for model 1 were from 6 to 12 percent greater than the values from the tunnel tests of reference 1

after the data were corrected for the mass flow of the flight model. The external drag of model 2 was 6 percent greater than that of model 1 at $M = 1.9$, 17 percent greater at $M = 1.3$, and 42 percent at $M = 0.9$. The wind-tunnel data of reference 2 indicated a 6-percent difference between similar configurations at $M = 2.01$. The minimum-drag coefficient of reference 6 agreed with the data of reference 2 at $M = 2.0$ but was slightly less than the data of reference 1 at $M = 1.6$. An estimate was made of the drag due to lift of the canard trimmers of model 2 when they were deflected $10°$ at subsonic speeds. This estimate, which did not account for interference effects, was only about one-third of the measured difference between model 1 and model 2.

The drag due to lift (fig. 13(a)) was obtained from the flight data for models 1 and 2 and compared with the tunnel test data of references 1 and 2. The reciprocal of the lift-curve slope was also included for comparison. The drag due to lift dC_D/dC_L^2 of both models 1 and 2 varied from 0.25 at $M = 1.0$ to 0.38 at $M = 2.0$. At subsonic speeds model 2 had more drag due to lift than model 1, apparently because model 2 required a larger angle of attack to produce the same lift coefficient. (See fig. 7.) As the data from the tunnel tests were compared with the flight-test data, fair agreement was noted near $M = 2.0$, but at $M = 1.4$ and 1.6, tunnel drag-due-to-lift values at zero deflection were about 15 percent lower than the flight-test data. From figure 13(b) it is interesting to note that the minimum drag occurred at a lift coefficient of zero at supersonic speeds and at a slightly negative lift coefficient at subsonic speeds. The canard trimmers of model 2 shifted the minimum point of the drag curves to a more negative lift coefficient than was obtained for model 1 at speeds less than $M = 1.5$. The maximum lift-drag ratio and the lift coefficient at which it occurred are shown in figures 13(c) and 13(d) for models 1 and 2. As evidenced by the agreement between the measured and the calculated data, the maximum lift-drag ratio varies parabolically and the calculated values probably represent the $(L/D)_{max}$ at zero elevon deflection even at the higher Mach numbers. Over the test Mach number range, $(L/D)_{max}$ varied from 4 to 6 and occurred at lift coefficients from 0.3 to 0.5.

Lateral Stability

A vector-analysis procedure was used to determine the lateral stability derivatives C_{Y_β}, C_{l_β}, C_{l_r}, and $C_{n_r} - C_{n_\beta}$ at $M = 1.8$ for model 3. However, lateral-stability data were not obtained at Mach numbers other than $M = 1.8$ since there was a good indication that the filling in the vertical tail progressively flaked off, causing trim changes of sufficient magnitude to motivate instability when the second pulse rocket ignited. Stability was regained almost immediately as a

high rate of roll was induced through the strong dihedral effect and sustained at a value near the natural yawing frequency of the nonrolling model; the associated cross-coupled motion between pitch and yaw was experienced during the remainder of the flight. The data used for the analysis of the first yaw disturbance are shown in figure 14, the equations of motion and their vector solutions at $M = 1.8$ in figure 15, the trim characteristics over the Mach number range in figure 16, and the divergence boundaries of model 3 in figures 17 and 18.

The motions of model 3 resulting from ignition of the first pulse rocket after the model separated from the booster were analyzed by the vector method outlined in the section entitled "Reduction of Data" and described in detail in reference 17. The measured data are shown by the time histories in figure 14. The average slope of the lateral-force coefficient C_{Y_β} for the portion analyzed was -1.63 per radian. By using these quantities, the mass characteristics of the model, and the equations of motion it was possible to construct the vector polygons shown in figure 15. All angles were used in radian measure. In the tables of figure 15 all vectors were considered positive and the sign of the scalars was included in the phase angle from β. There were three unknowns in the rolling-moment equation, but since the directions of the vectors were known the magnitude of these vectors could be determined by assuming a value for the third. Because some unpublished tunnel data were available, the damping-in-roll derivative C_{l_p} was esti-mated to be -0.404 per radian for model 3 and was used in the roll diagram in lieu of C_{l_r} or C_{l_β}. Solving the vector diagram for C_{l_r} and C_{l_β} yielded values of -1.13 and -0.308 per radian, respectively, for $M = 1.8$. A similar situation existed in the yawing-moment equation; C_{n_β} and $C_{n_r} - C_{n_{\dot\beta}}$ were determined for three assumed values of C_{n_p}. The damping-in-yaw derivative $C_{n_r} - C_{n_{\dot\beta}}$ varied from about -5.0 to -6.0; however, C_{n_β} remained nearly constant at 1.3 for the same range of C_{n_p}. The static derivatives C_{Y_β}, C_{n_β}, and C_{l_β} were all large compared with the tunnel data for the basic configuration as shown in reference 1. As would be expected, the dynamic derivatives were also large since the total area of the vertical tail was more than doubled.

The trim angle of attack, the trim angle of sideslip, and the trim lateral-force coefficient of model 3 are shown in figure 16. These data were compared with data from model 1 to help to illustrate the sequence of events that motivated the unforeseen behavior of model 3 during its flight. Models 1, 2, and 3 all vibrated at the organ-pipe frequency of the plugged duct while attached to the booster. This

shaking action subsided on models 1 and 2 at the time of separation; however, it continued for model 3, at a higher frequency, until shortly after the second pulse-rocket disturbance. Prior to the flight test of model 3, the model was vibrated on an electrodynamic exciter to determine its natural structural frequencies and modes of vibration. It was found that the vertical tail resonated in bending, with a nodal line near the fuselage, at a frequency identical to the frequency later measured during the boosted portion of the flight. The vibrations on the booster were probably severe enough to shake some of the filler from the undercut on the right side of the vertical tail (see fig. 2(d)), and the resulting cavities may have induced buffet at some speeds after separation. Because of the flexibility of the vertical fin, tail loads resulting from the yaw disturbances would also tend progressively to flake out the filler. Evidence of this is shown in figure 16 by the steplike changes in the trim angle of sideslip; such trim changes were not experienced by model 1 as it coasted to decreasing Mach numbers. Corresponding to these trim changes, predominant deviations were measured in the mean values of rolling acceleration. Thus it appeared that the steady-state rolling velocity was established by the out-of-trim in sideslip through the strong dihedral effect of the oversized vertical tail within the first few seconds after booster separation $\left(C_{l_\beta} = -0.3\right.$ at $M = 1.8\bigr)$. The first pulse rocket disturbed the model in the direction of positive β and the roll rate reduced almost instantaneously. (Compare the steady-state roll rate of figure 18 with trim of fig. 16.) However, between the first and second pulse rockets the trim angle of sideslip increased negatively with a corresponding increase in roll rate. By the time the second pulse rocket ignited (at $M = 1.61$), the roll rate had increased to a steady-state value of 10 radians per second. The disturbance from this pulse rocket caused the model to yaw to negative angles, which further increased the roll rate to a maximum steady-state value of nearly 50 radians per second. Transient rates exceeded 85 radians per second. For the remainder of the flight, model 3 oscillated as though it were statically and dynamically stable although the motion was strongly coupled between the pitch and yaw planes and large trim changes were noted in all the measured quantaties. (See fig. 16.) Since the influence of the vertical tail with part or all of the filler removed was not known, and since some of the instruments were subjected to quantities greater than six times their calibrated range at the maximum roll rates, the cross-coupled motions were not analyzed.

Divergence boundaries of model 3 were calculated by the method of reference 12 and are shown in figure 17 at $M = 1.6$. Boundaries between stable and unstable regions were calculated by using experimental pitch parameters and estimated yaw parameters with a pitch damping of 5.5 percent of critical and yaw damping of 6.6 percent of critical. The nondimensional undamped natural frequencies in pitch and in yaw for the nonrolling missile, ω_θ and ω_ψ, were calculated for model 3 at $M = 1.6$

for various roll rates from the parametric equations shown in figure 17. The diagonal line in the boundary plot indicates the model stability for various roll rates. It was found that model 3 was dynamically unstable for roll rates between 31.4 and 38.8 radians per second but stable both above and below these rates. The rolling velocities required to produce resonance in pitch and yaw when damping is neglected $\left(\omega_\theta = \omega_\psi = 1\right)$ were estimated for the test Mach number range and are presented in figure 18 with the measured roll rates. The stability boundaries without damping (fig. 18) were very close to the values calculated with damping (fig. 17). After the model reached angular velocities in roll greater than the non-rolling yawing frequency, the response resulting from the remaining pulse rockets was not large enough to reduce the roll rate sufficiently to pass through the unstable region. Since the steady-state roll rate was sustained at relatively high values (greater than 20 radians per second), the cross-coupled motions persisted for the remainder of the flight.

SUMMARY OF RESULTS

The following results were obtained from flight tests, over a Mach number range of $M = 0.8$ to $M = 2.1$, of five 0.12-scale models of the Regulus II missile for a center of gravity located 45 percent of the mean geometric chord ahead of its leading edge:

1. Model lift, both with and without canard trimmers, was linear with angle of attack and the lift-curve slope decreased from 0.065 at $M = 1.0$ to 0.041 at $M = 2.0$.

2. The aerodynamic-center location of the basic configuration was constant at 35 percent of the mean geometric chord at supersonic speeds and about 10 percent at $M = 0.90$. Canard trimmers reduced the static stability about 15 percent at supersonic speeds.

3. The models were dynamically stable, and although the damping was good for a tailless configuration it was still low - 5 to 6 percent of critical damping.

4. The large negative pitching moment at zero lift measured on the basic configuration at supersonic speeds was reduced to nearly zero by the addition of canard trimmers. However, at low transonic speeds the trimmers caused a negative increase in the zero-lift pitching moment.

5. At $M = 1.9$ the mass-flow ratio of the duct based on the cross-sectional area of the duct projected to the inlet lip was unity, with a pressure recovery of 86 percent. Although the canard trimmers had little influence on the duct above $M = 1.6$, they improved the performance by nearly a constant amount at Mach numbers less than 1.6.

6. The minimum external-drag coefficient of the basic configuration was 0.024 at $M = 0.8$, 0.045 at $M = 1.3$, and 0.033 at $M = 2.1$. Canard trimmers caused an increase varying from 6 percent at $M = 1.9$ to 42 percent at $M = 0.9$.

7. Vector solutions of the lateral motions of a model with a vertical tail twice as large in area as that of the basic configuration produced relatively large, stable values of both static and dynamic derivatives at $M = 1.8$.

Langley Aeronautical Laboratory,
    National Advisory Committee for Aeronautics,
        Langley Field, Va., July 29, 1958.

DECLASSIFIED

APPENDIX

ACCURACY

The method used to estimate the accuracy of the data was obtained from the chapter entitled "The Precision of Measurements" in reference 14. In this analysis, probable error was used to indicate the accuracy of the results.

If a large number of direct measurements are made of a single quantity, and all deviations from some reference are noted, the magnitude of the probable error r may be defined as such that half of the total number of deviations are greater than r and half are less than r. That is, the probability that the error of a single measurement will fall between +r and -r is one-half.

It was assumed that the flight measurements had a probable error of $\pm 1/2$ percent of the calibrated instrument range. Mach number was also assumed to be a direct measurement to facilitate calculations. This assumption was justified by the fact that Mach numbers closely agreed when calculated from two nearly independent sets of measurements: from model stagnation pressure in conjunction with rawinsonde static pressure, and from CW Doppler velocity in conjunction with rawinsonde speed of sound. The probable error in Mach number then was estimated from the assumed errors in rawinsonde static pressure and model stagnation pressure. The assumed probable errors of the directly measured quantities are shown in table V.

From reference 14, the probable error of the indirect measurements, such as the final data, may be estimated by the following equation:

$$R = \sqrt{\left(\frac{\partial Q}{\partial q_1}\right)^2 r_1{}^2 + \left(\frac{\partial Q}{\partial q_2}\right)^2 r_2{}^2 + \left(\frac{\partial Q}{\partial q_3}\right)^2 r_3{}^2 + \ldots + \left(\frac{\partial Q}{\partial q_n}\right)^2 r_n{}^2} \qquad (A1)$$

where R is the probable error of the indirect quantity Q, and Q is a function of the direct measurements q_1, q_2, q_3, . . . q_n, each with a probable error of r_1, r_2, r_3, . . . r_n. In order to apply equation (A1), the relation between the direct measurements and the final results must be established mathematically. For instance, the lift-curve slope was measured directly from a plot of C_L against α, but for error calculations it was first necessary to assume the equation of a line passing through at least two representative points from the measured data, and then to express the slope of this line with respect to normal acceleration,

longitudinal acceleration, angle of attack, Mach number, static pressure, model weight, and wing area. This facilitates the partial differentiation of C_{L_α} with respect to the independent variables, as required for equation (A1). A similar technique was used for the final data, and the estimated errors are shown in table V.

DECLASSIFIED

WING:

Span	:	28.55
Mean geometric chord .	:	10.47
Thickness, percent c .	:	4.00°
Leading-edge sweep . .	:	46.14°
Aspect ratio	:	2.73
Taper ratio	:	0.60
Total area, sq ft . . .	:	2.08

VERTICAL TAIL:

Span	:	9.36
Mean geometric chord .	:	9.64
Thickness, percent c .	:	4.00
Leading-edge sweep . .	:	60.00°
Aspect ratio	:	1.12
Taper ratio	:	0.33
Total area, sq ft . . .	:	0.54

VENTRAL FIN:

Same as vertical tail about
model center line.

Total-pressure pickup

α-β Indicator

Station 0

Sta. 81.50
Sta. 68.37
Sta. 64.00 Pulse rocket
Sta. 44.73
Sta. 40.00 Model center of gravity
Sta. 36.54
Sta. 27.72
Sta. 22.25 Pulse rockets
Sta. -12.00

0.45
0.52
8.55 (max.)
6.00 (max.)

(a) Model 1.

Figure 1.— General arrangement of 0.12-scale flight models of Regulus II. All dimensions are in inches.
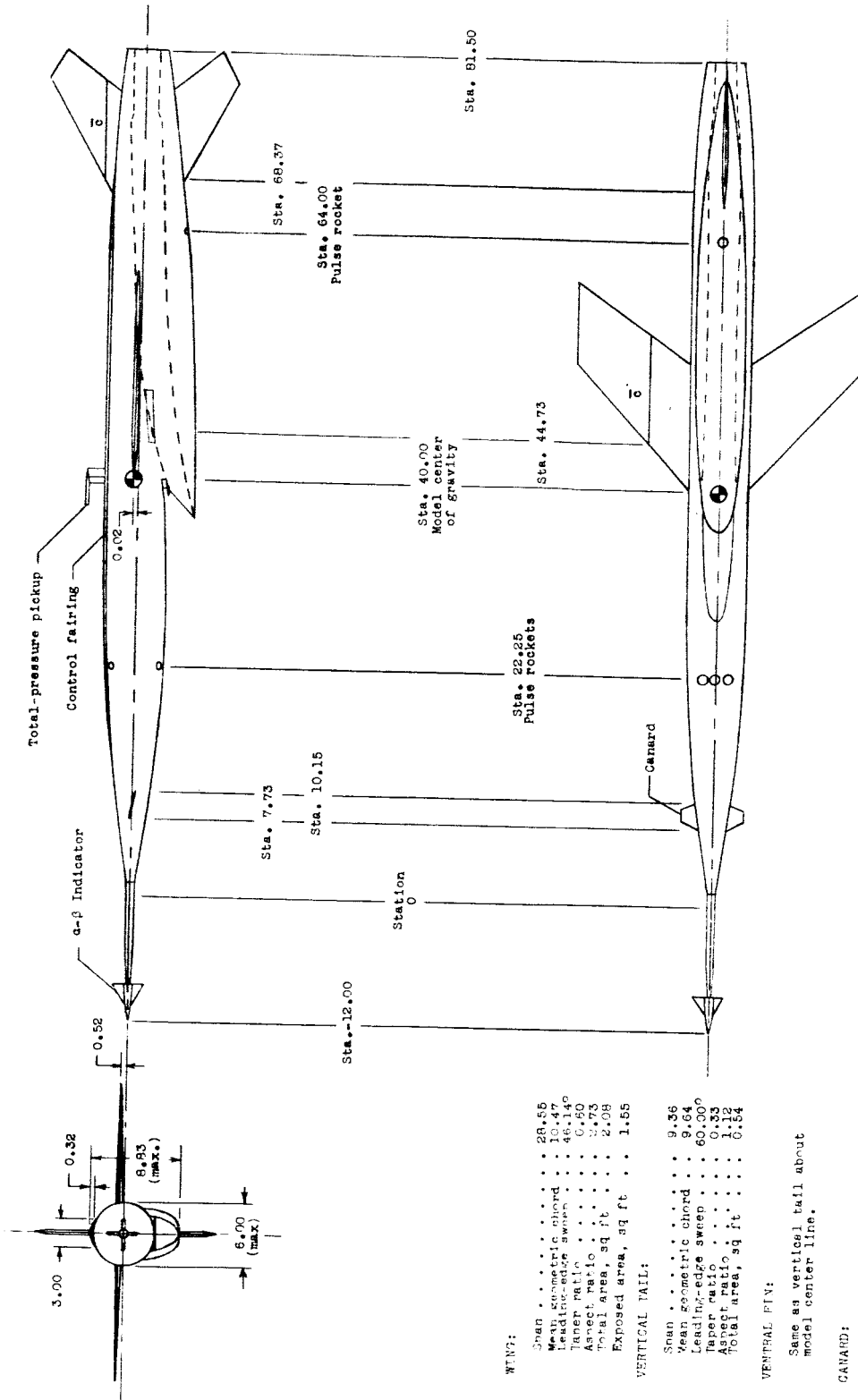
DECLASSIFIED

(b) Model 2.

Figure 1.- Continued.
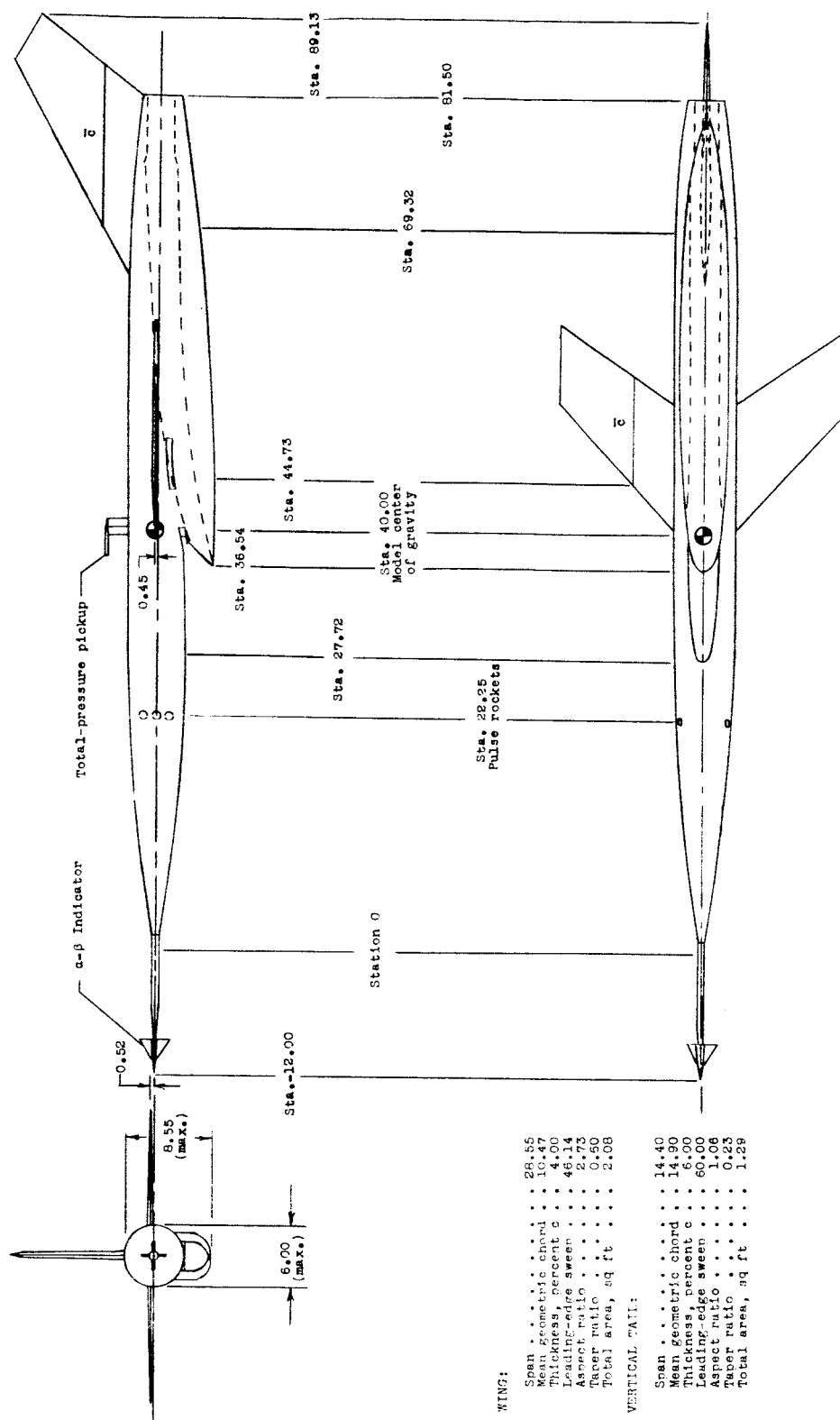
(c) Model 3.

Figure 1.- Continued.

CONFIDENTIAL

Sta. 81.50

Sta. 68.37

Sta. 44.73

Sta. 33.48
Model center
of gravity

Station
0

0.25

Total pressure
for smokepot

0.52

8.55
(max.)

6.00
(max.)

WING:

Span	29.55
Mean geometric chord .	10.47
Leading-edge sweep . .	45.14°
Taper ratio	0.50
Aspect ratio	2.73
Total area, sq ft . .	2.08

VERTICAL TAIL:

Span	9.36
Mean geometric chord .	9.64
Leading-edge sweep . .	60.000
Taper ratio	0.33
Aspect ratio	1.12
Total area, sq ft . .	0.54

(d) Models 4 and 5.

Figure 1.- Continued.

DECLASSIFIED

Sta. 40.00
Model center
of gravity

Manifolded static
pressure orfices

15.25

14.53

Manifolded base
pressure orifices

3.46

2.22°

43.75° 14.25°

Integrating total-pressure rake

Base area 7.09 in.²

1.38   1.70

2.92

Station
0

0.52

1.77

2.42

10.15

10.0°

0.16

0.17

α-β Indicator sting
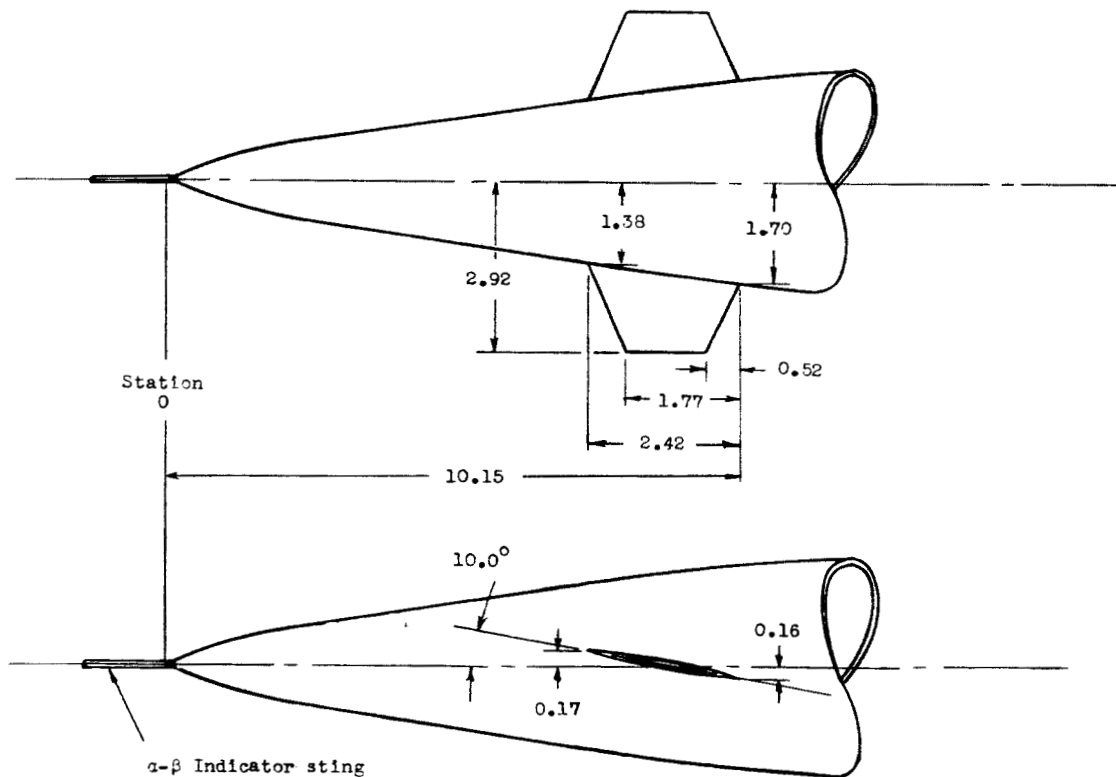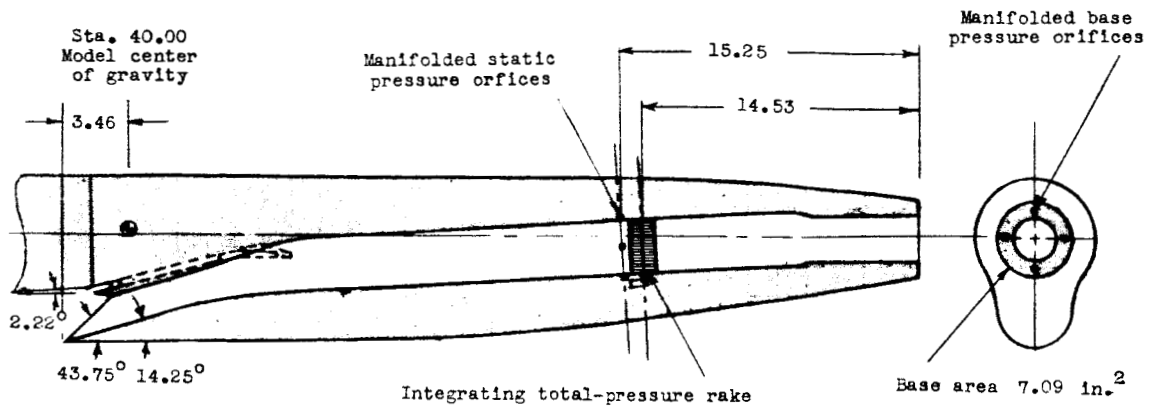
(e) Details of duct and canard trimmers.

Figure 1.- Concluded.

DECLASSIFIED
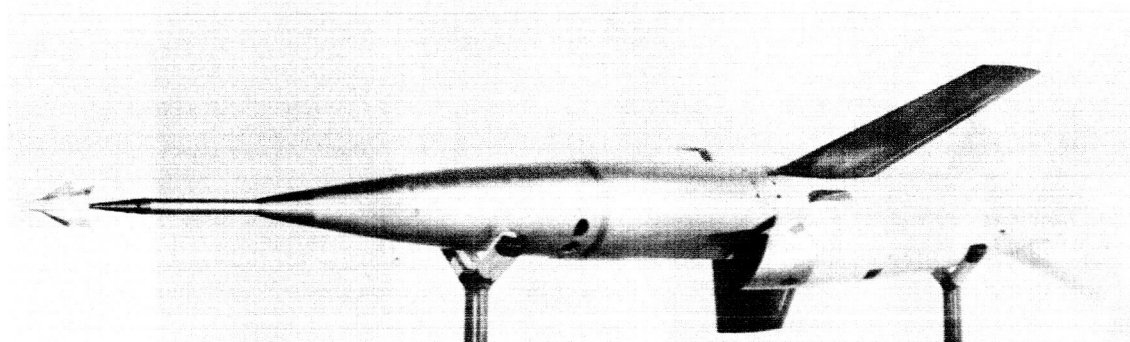
(a) Model 1, three-quarter front view.   L-35685
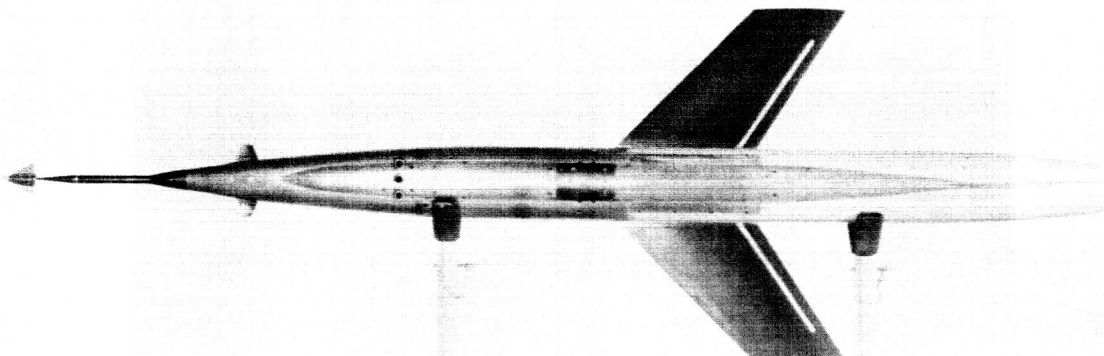
(b) Model 2, top view.   L-90189
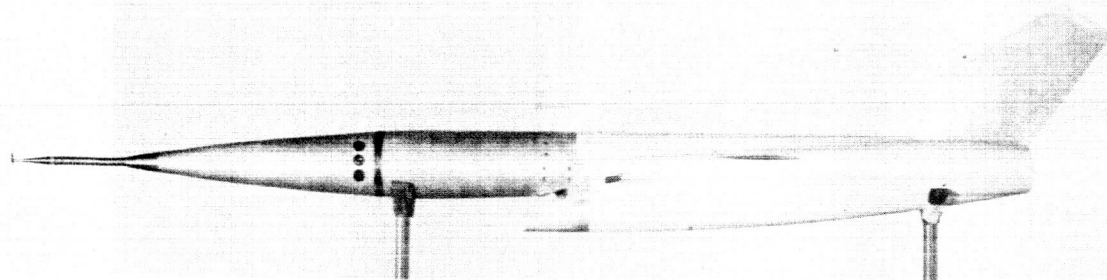
(c) Model 3, side view.   L-86786

Figure 2.- Photographs of models.
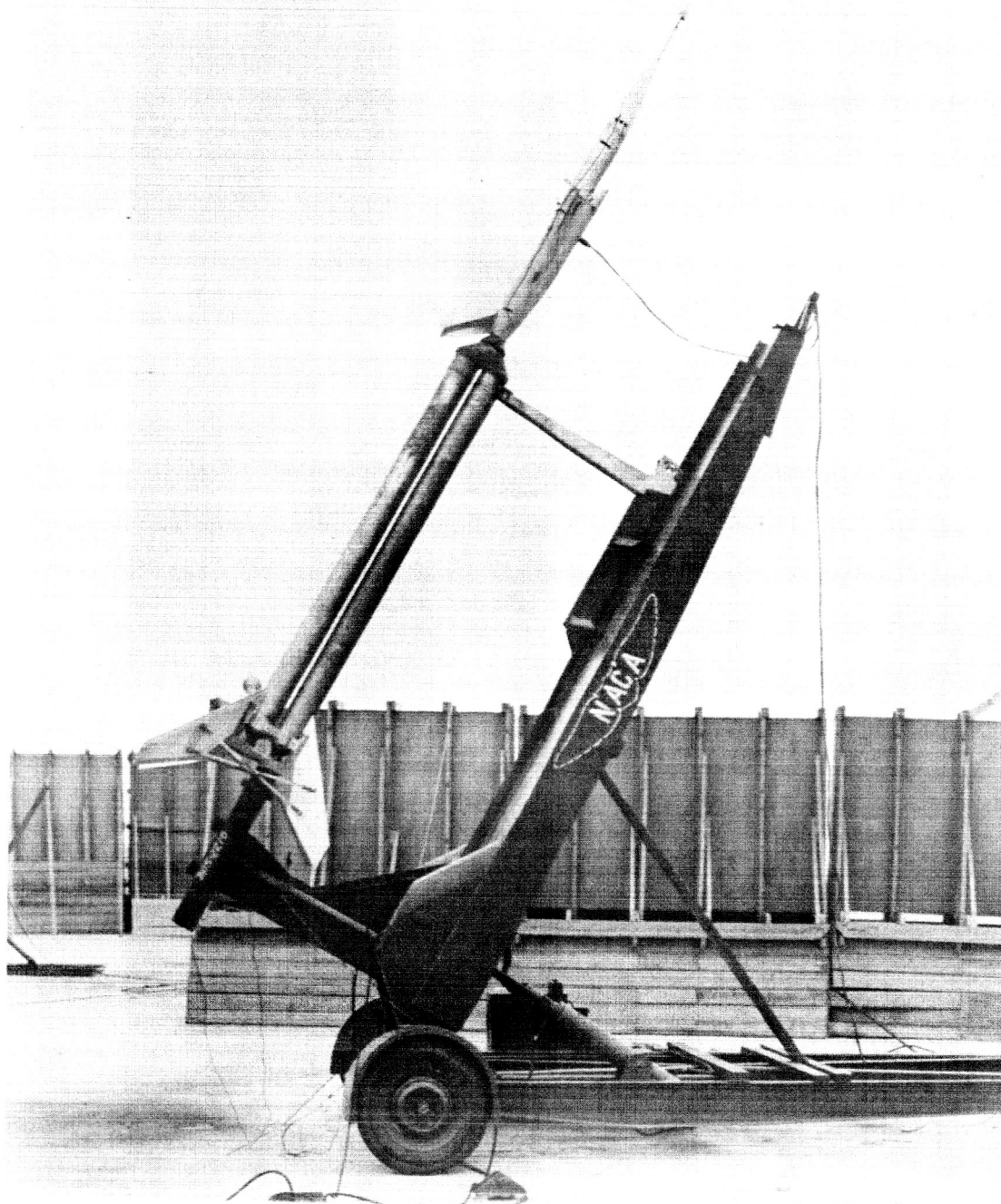
(d) Model 3 on launcher.   L-87268

Figure 2.- Concluded.
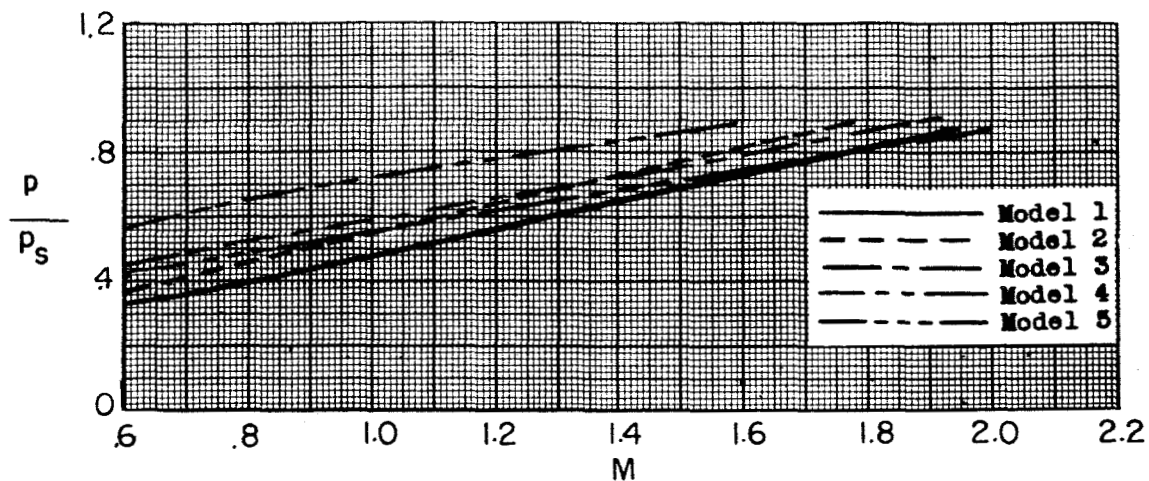
(a) Static-pressure ratio.
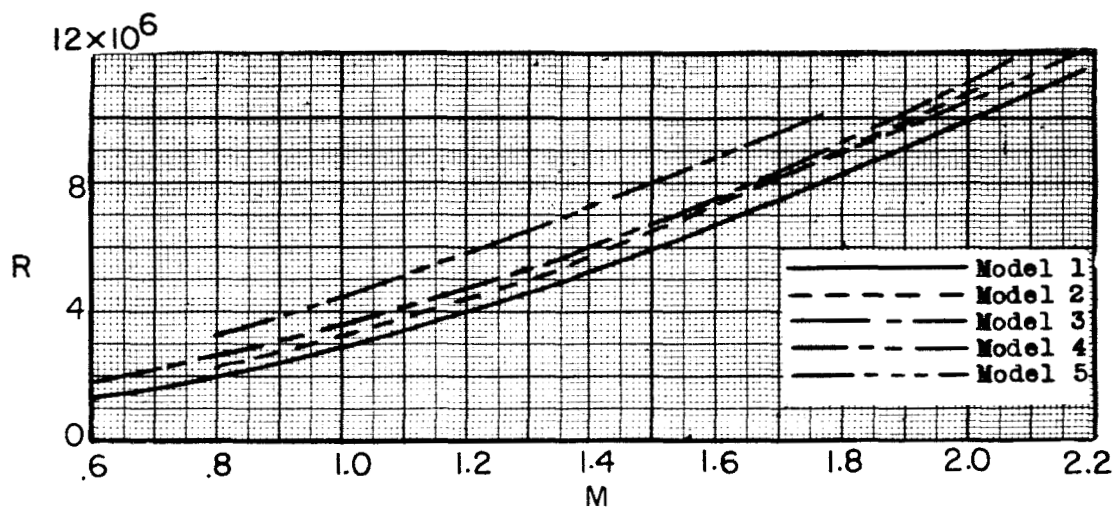
(b) Reynolds number, based on $\bar{c}$.
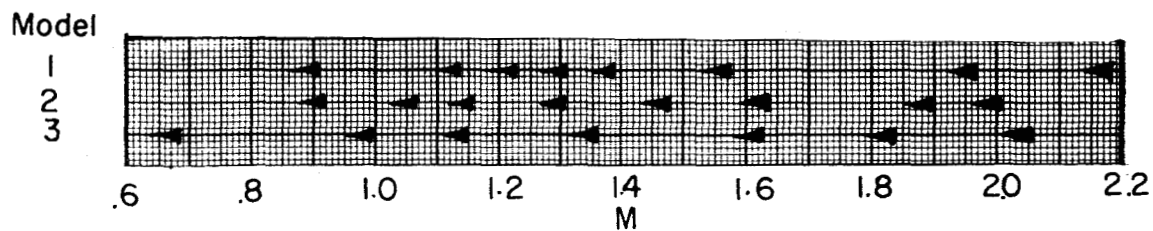
(c) Regions where disturbed models oscillated.

Figure 3.- Flight-test conditions.
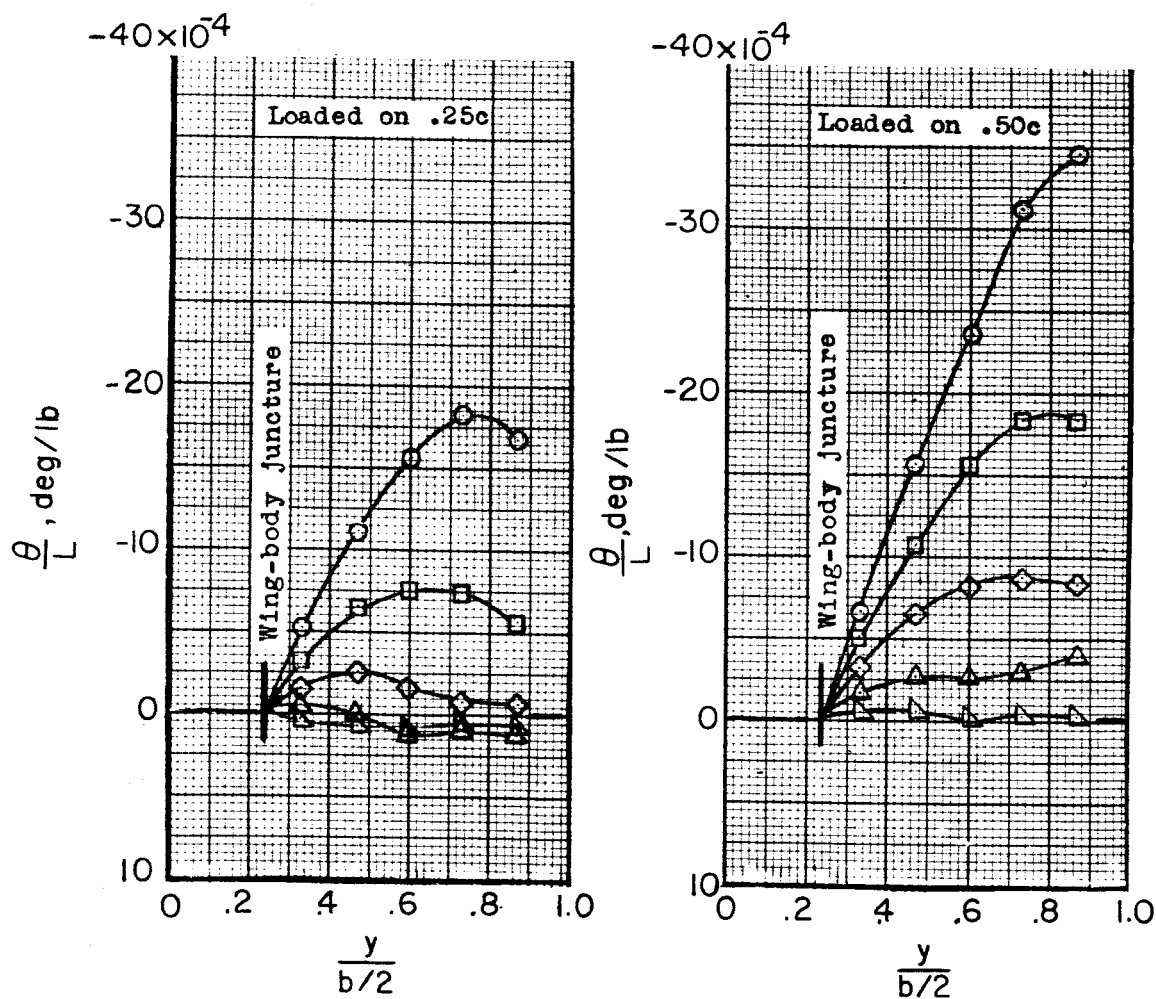
(a) Wing of models 1, 2, and 3.

Figure 4.- Structural influence coefficient.

DECLASSIFIED

Loading Stations

O .816 b
□ .657 b
◇ .499 b
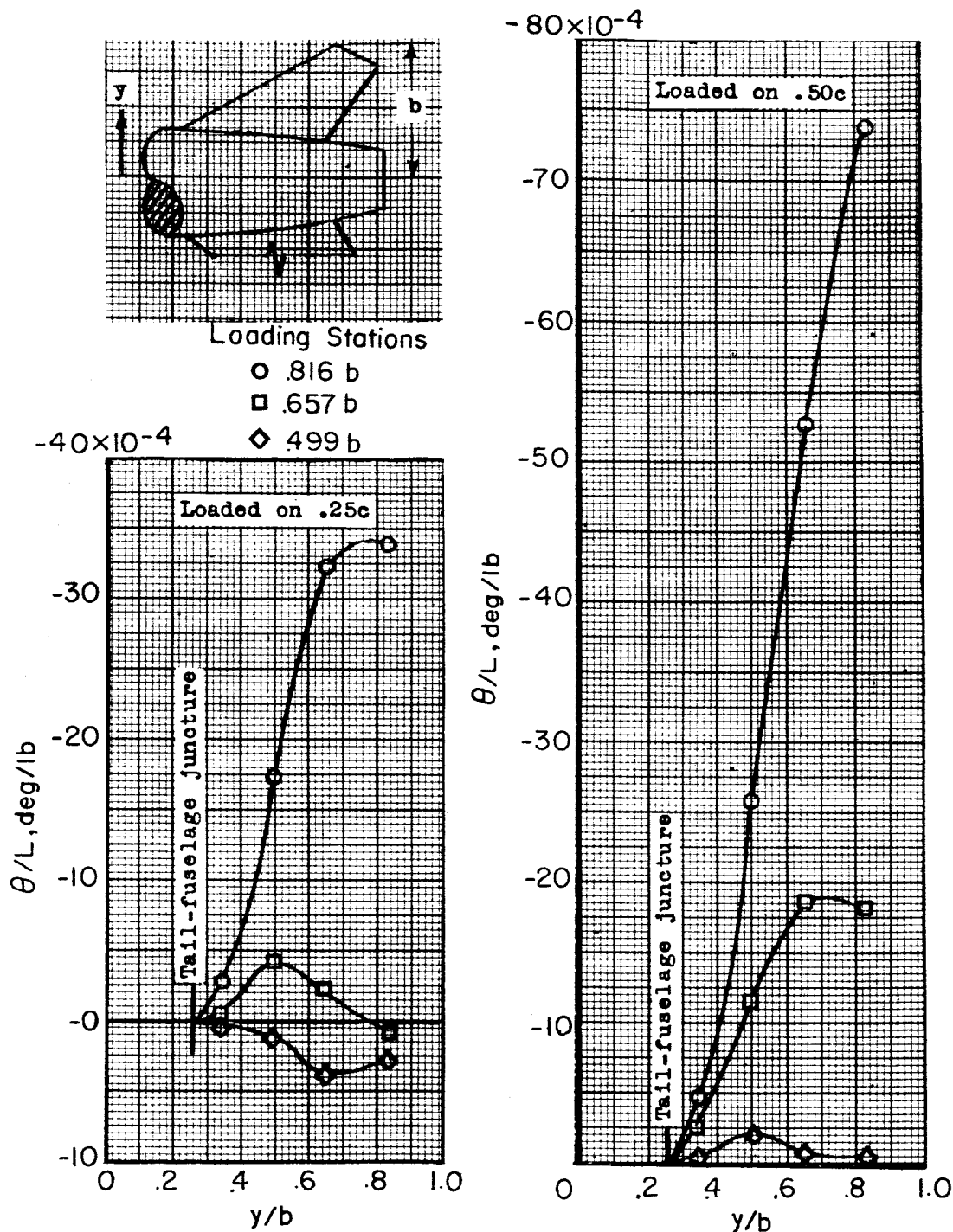
(b) Vertical tail of models 1 and 2.

Figure 4.- Continued.
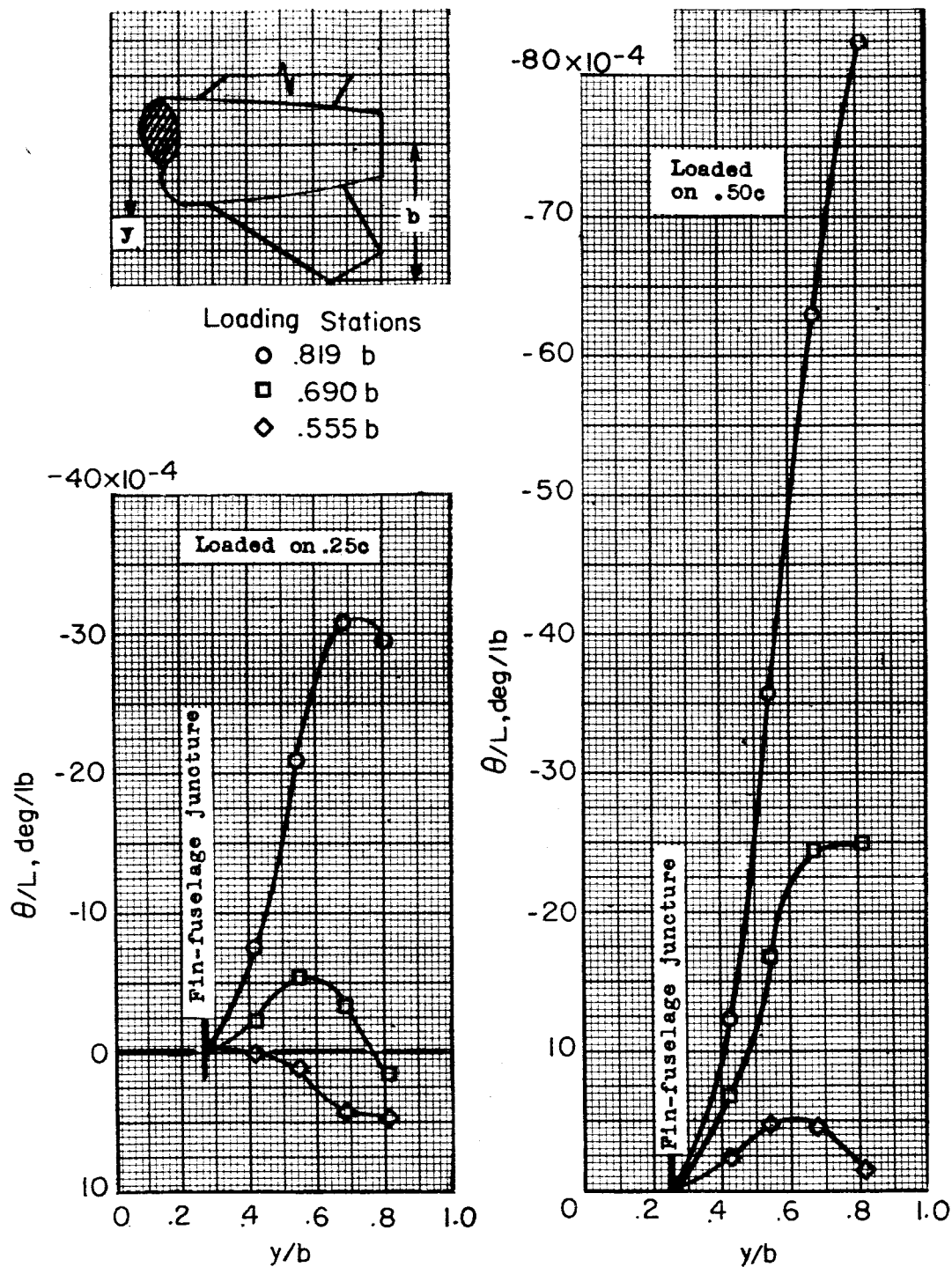
(c) Ventral fin of models 1 and 2.

Figure 4.- Continued.
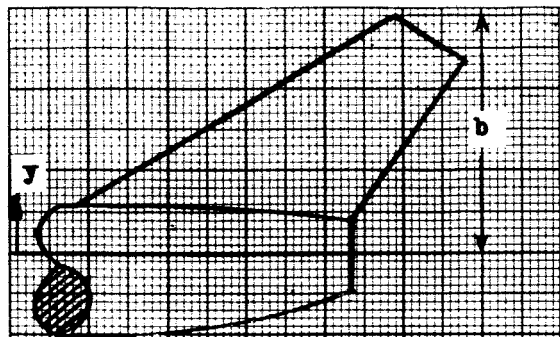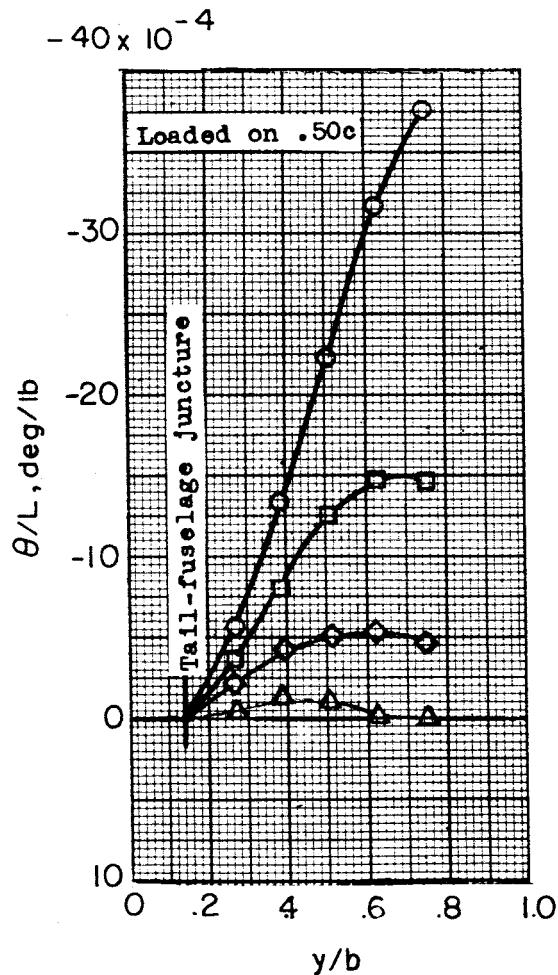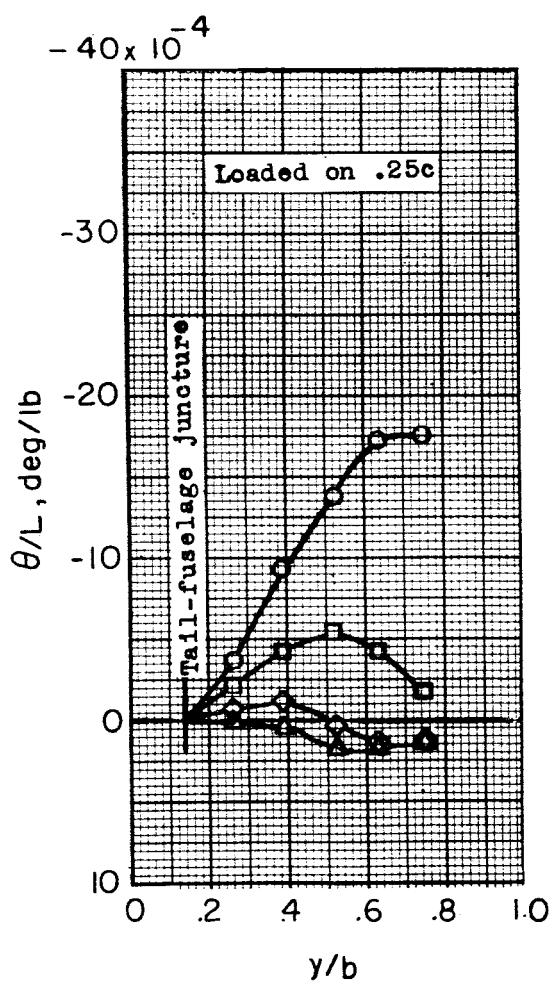
(d) Vertical tail of model 3.

Figure 4.- Concluded.
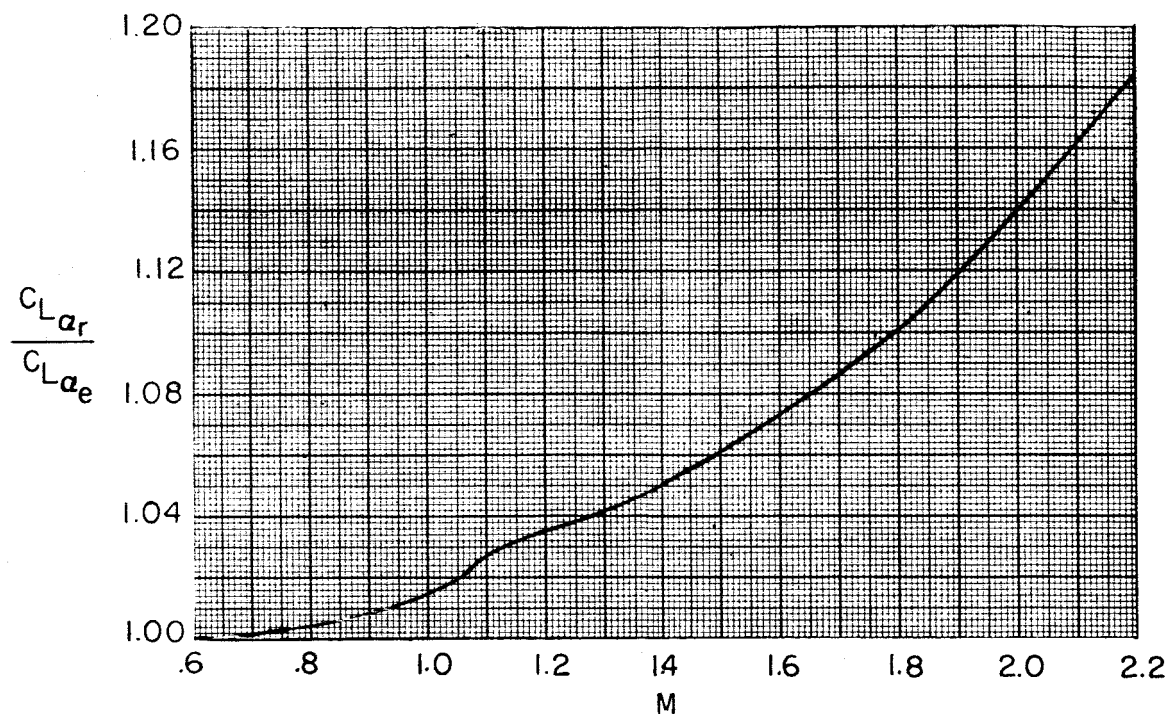
(a) Ratio of rigid to elastic lift.
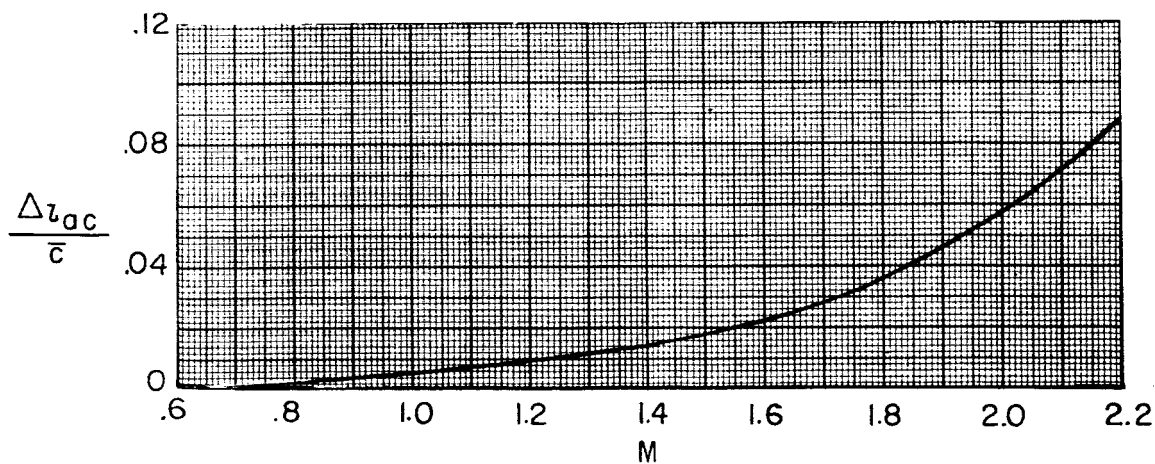
(b) Forward shift in aerodynamic center due to flexibility.

Figure 5.- Estimated aeroelastic properties of wing for models 1, 2, and 3.
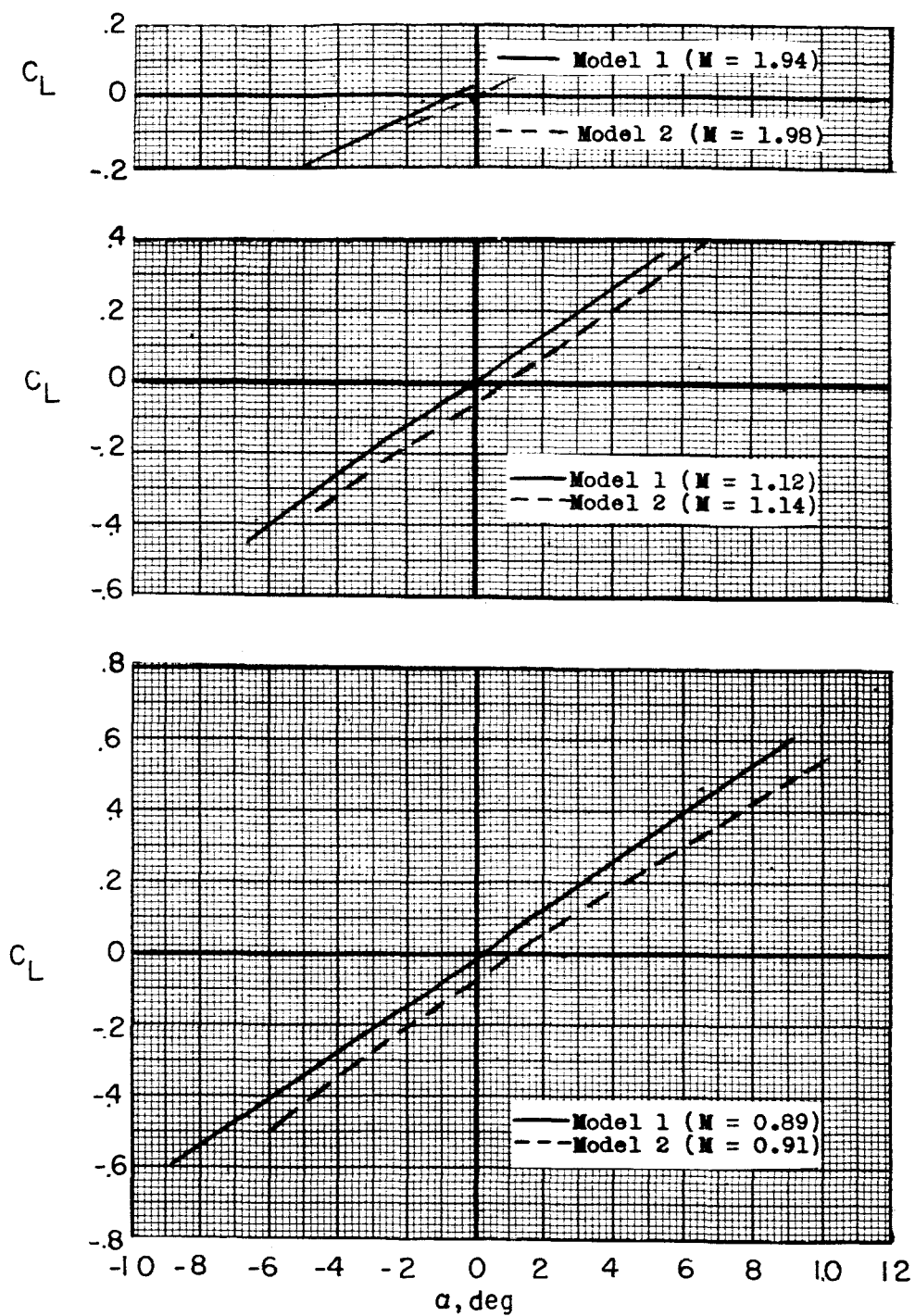
(a) Lift.

Figure 6.- Samples of measured data in nondimensional form.
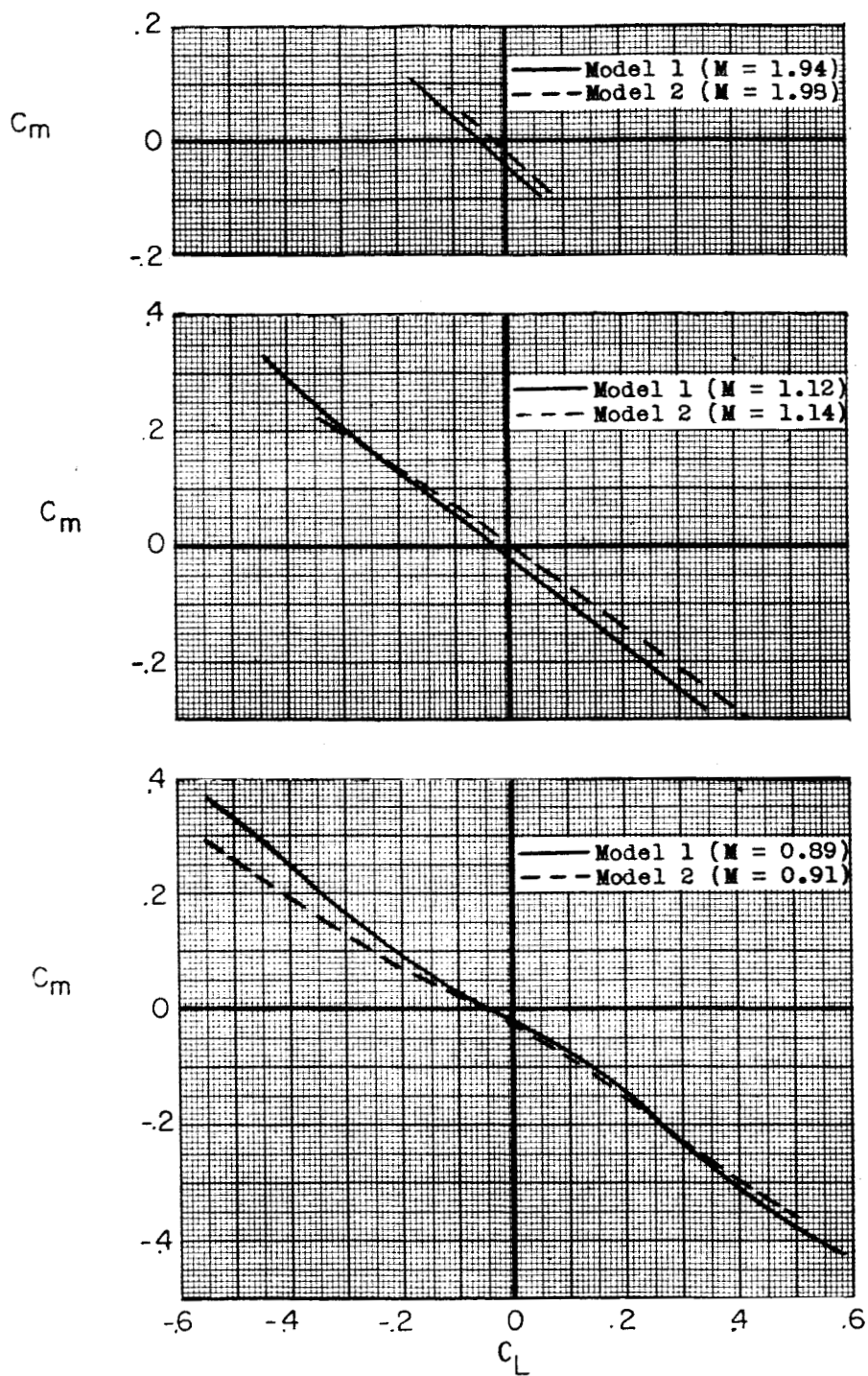
(b) Pitching moment.

Figure 6.- Continued.
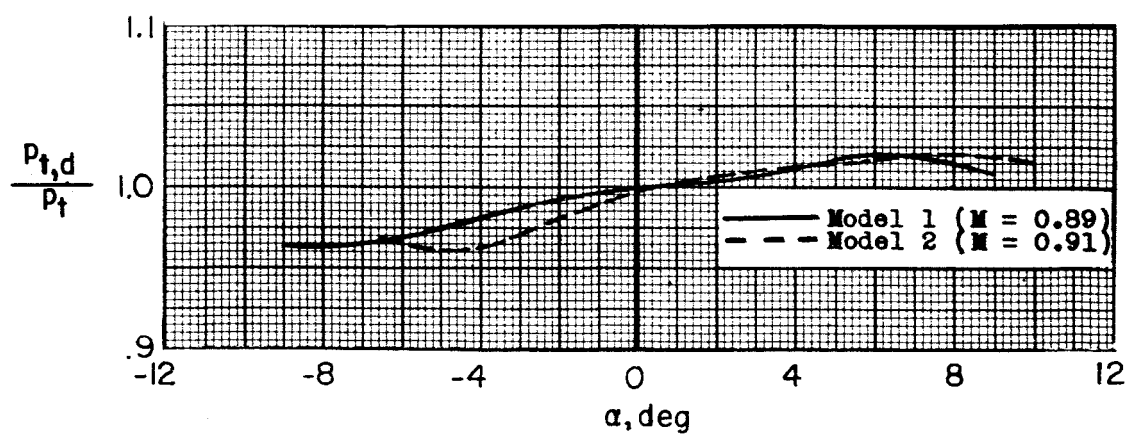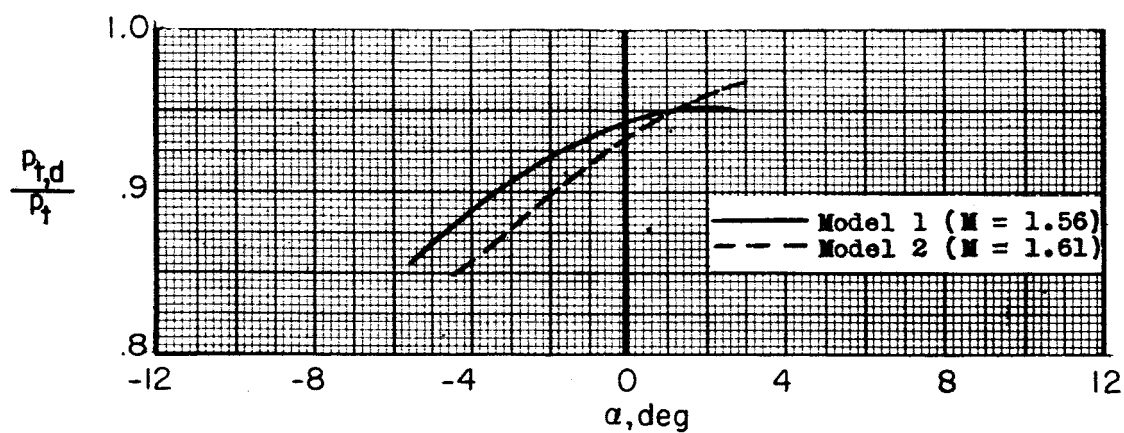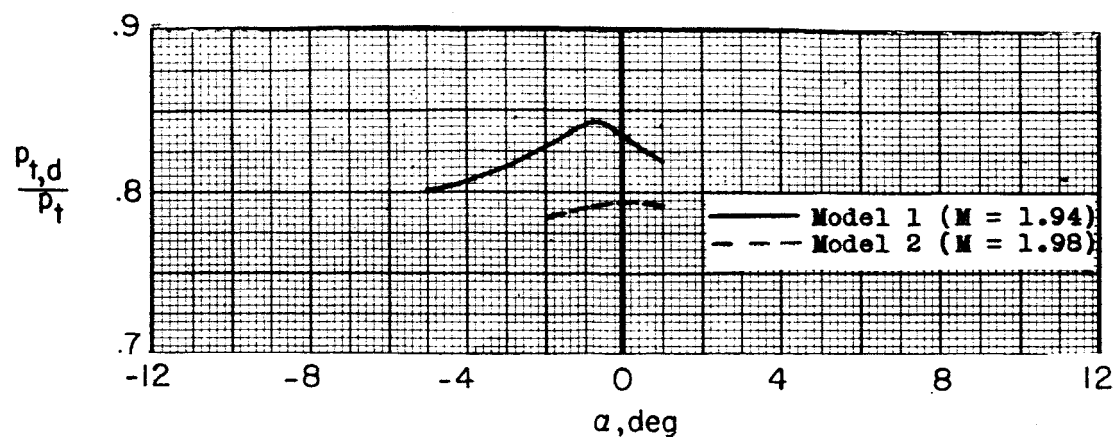
(c) Total-pressure recovery of duct.

Figure 6.- Continued.
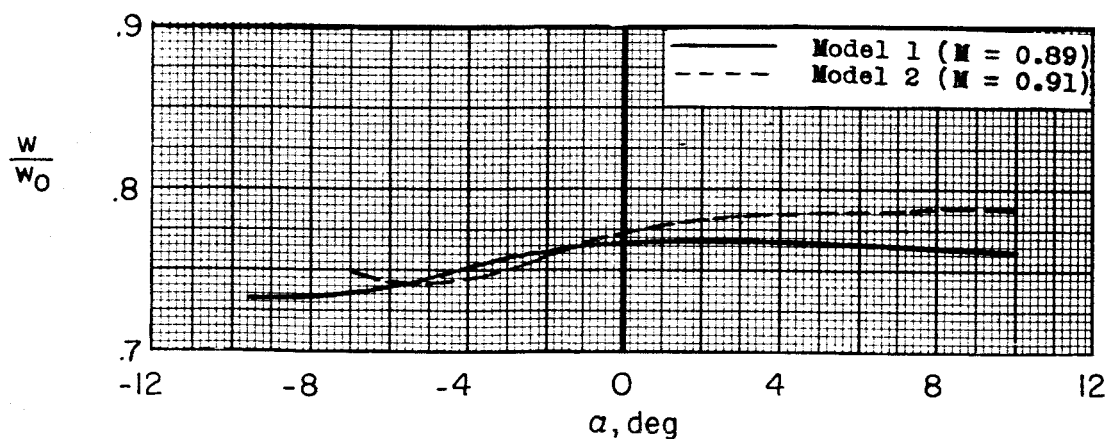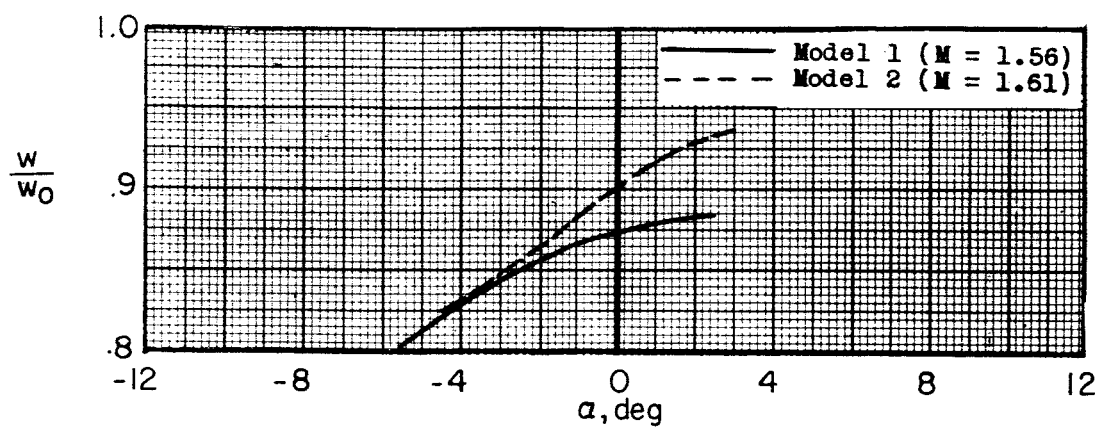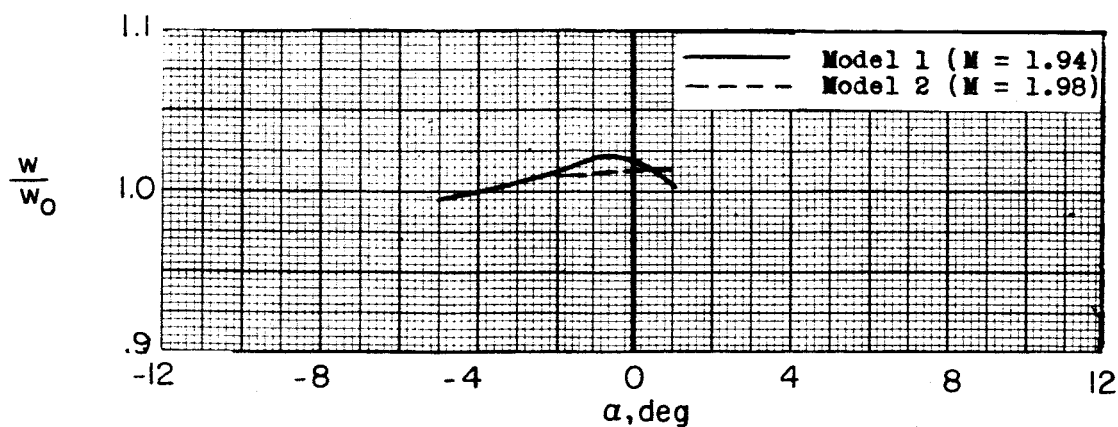
(d) Mass-flow ratio.

Figure 6.- Continued.

CONFIDENTIAL
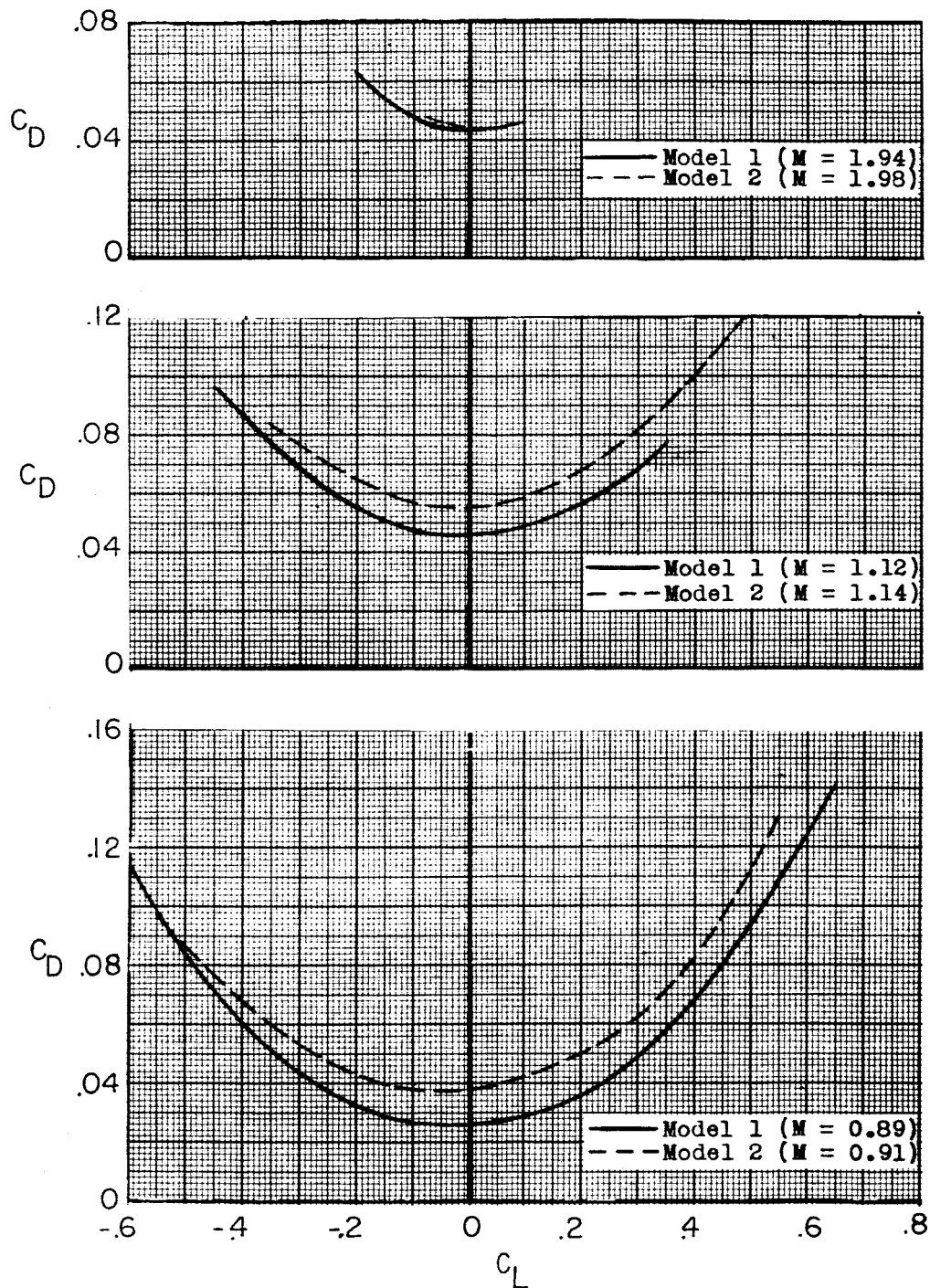
(e) Drag.

Figure 6.- Concluded.
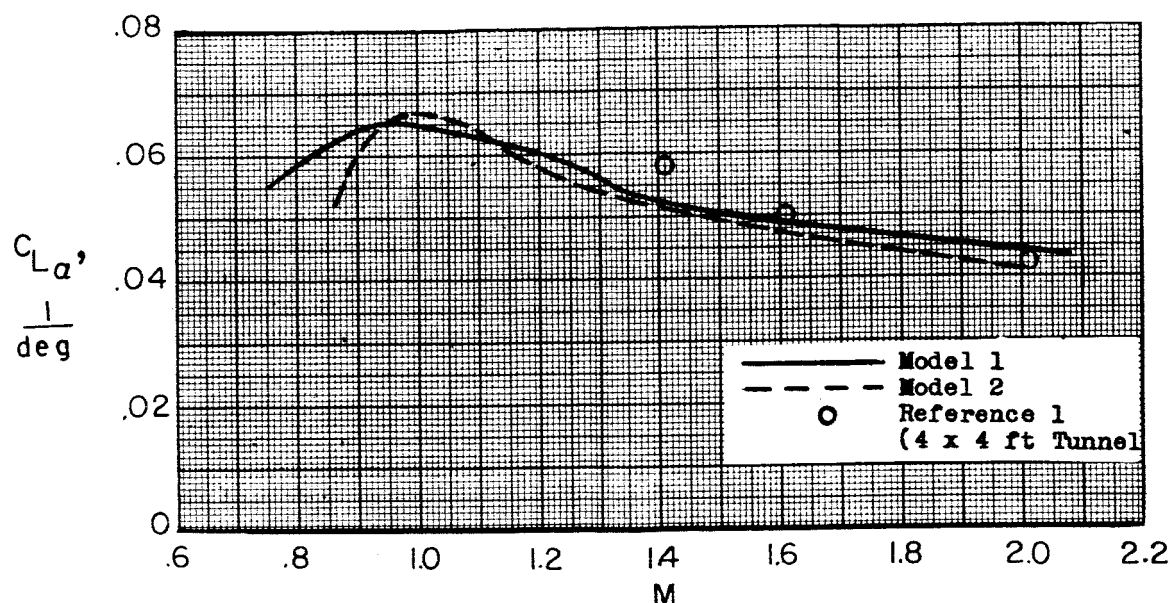
Figure 7.- Variation of lift-curve slope with Mach number.
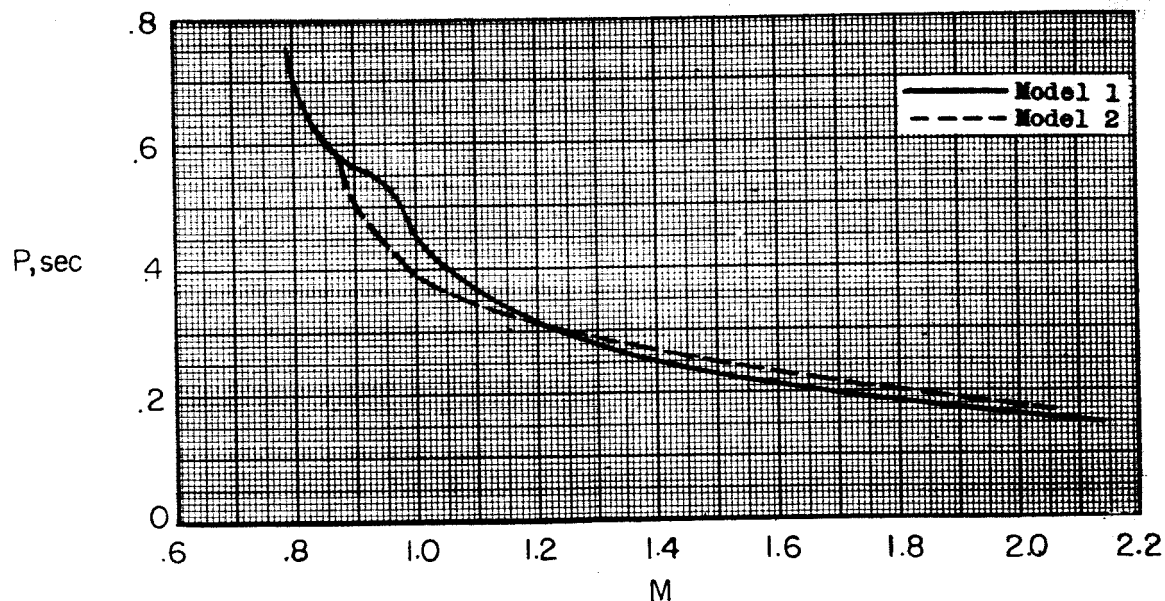
(a) Period of longitudinal oscillations.

Figure 8.- Variation of static longitudinal stability parameters of models 1 and 2 with Mach number. Center of gravity located $0.45\bar{c}$ ahead of $\bar{c}$.
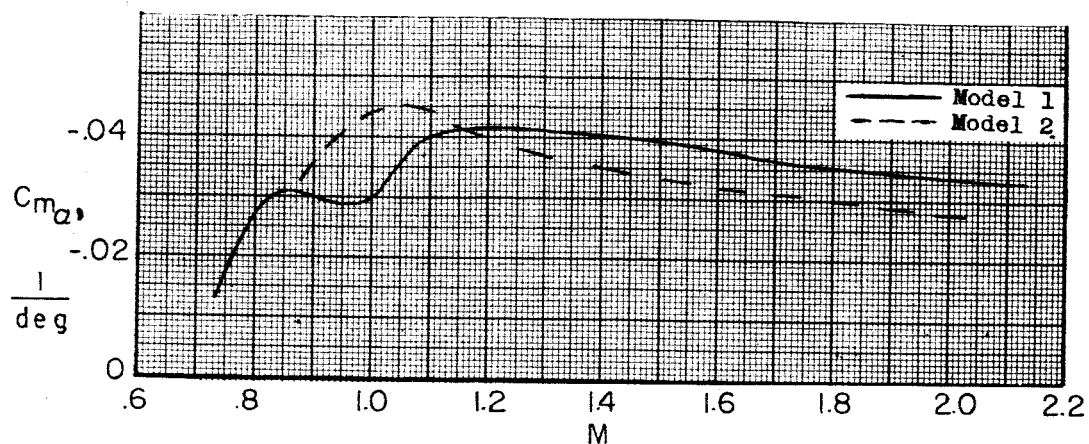
(b) Static-stability derivative.
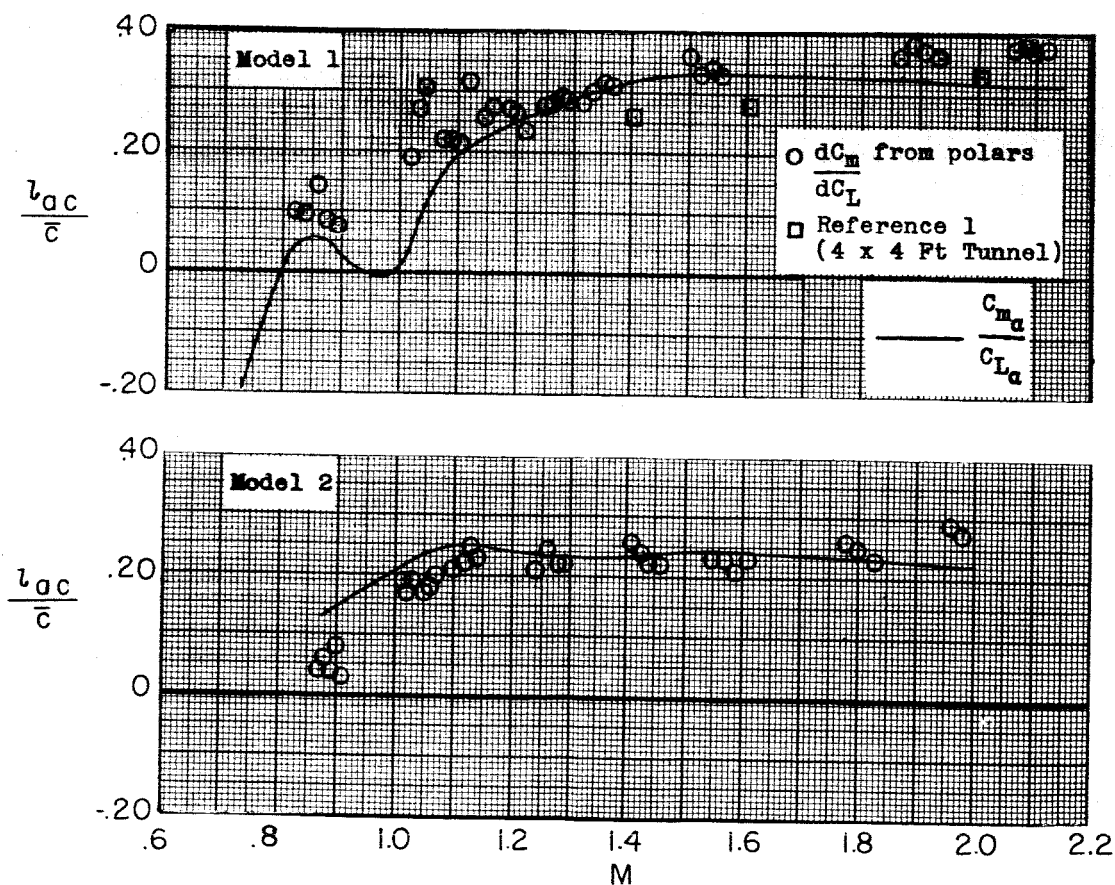
(c) Aerodynamic center.

Figure 8.- Concluded.

t_{y_2}, sec

Model 1
Model 2

M

(a) Time to damp to one-half amplitude.

$(C_{m_q} + C_{m_{\dot{\alpha}}})$,

$\frac{1}{rad}$

Model 1
Model 2

M
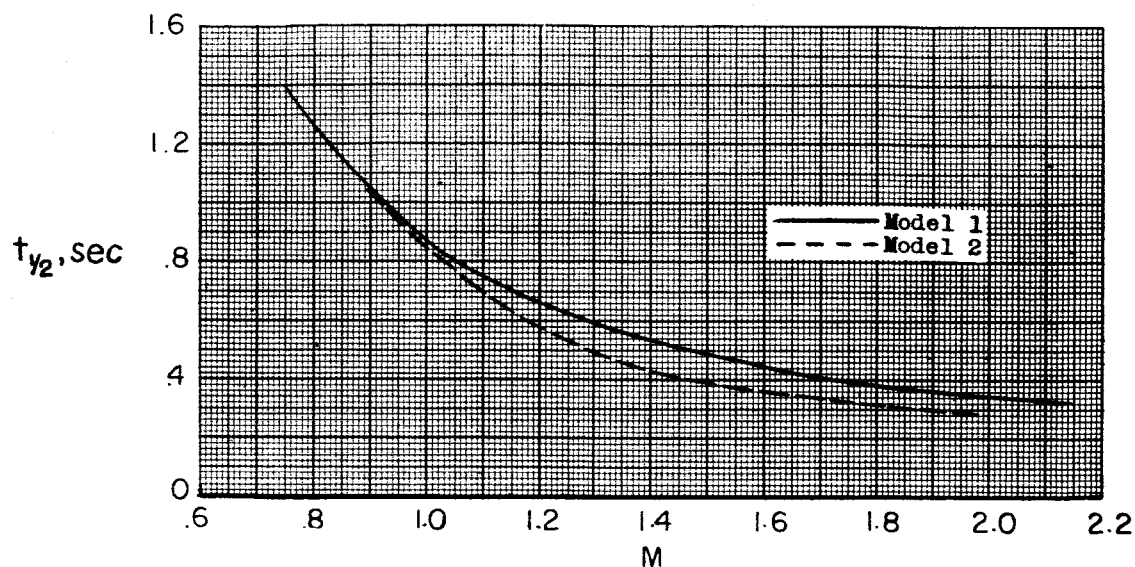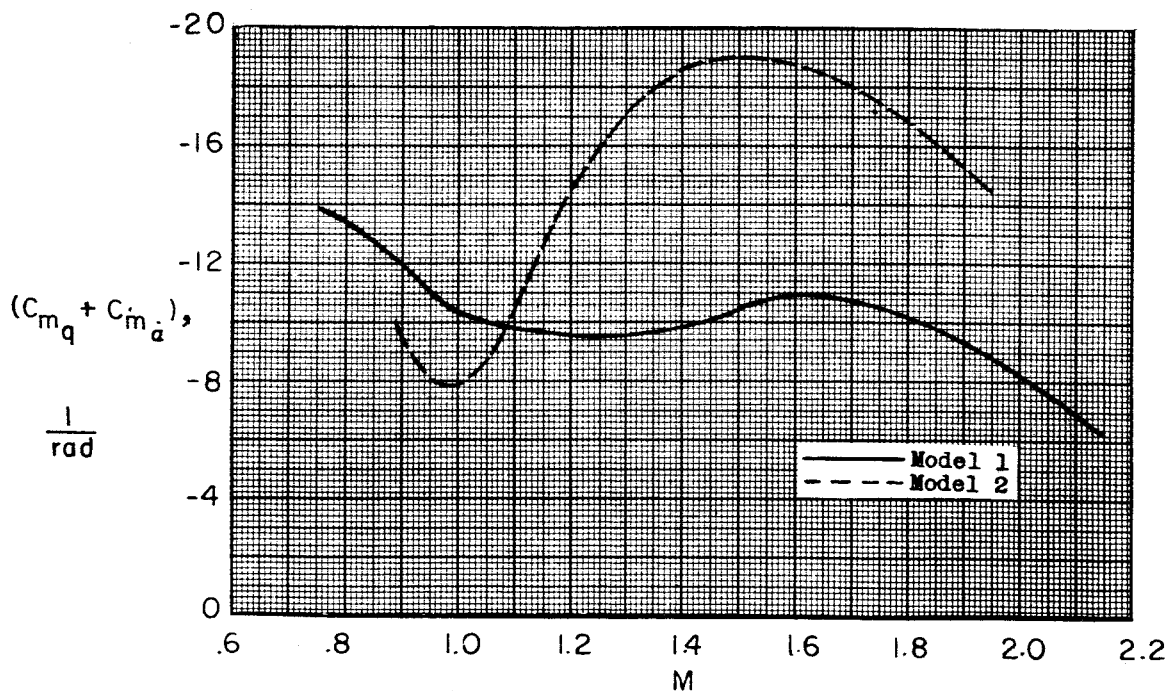
(b) Damping-in-pitch derivative.

Figure 9.- Variation of damping parameters with Mach number.
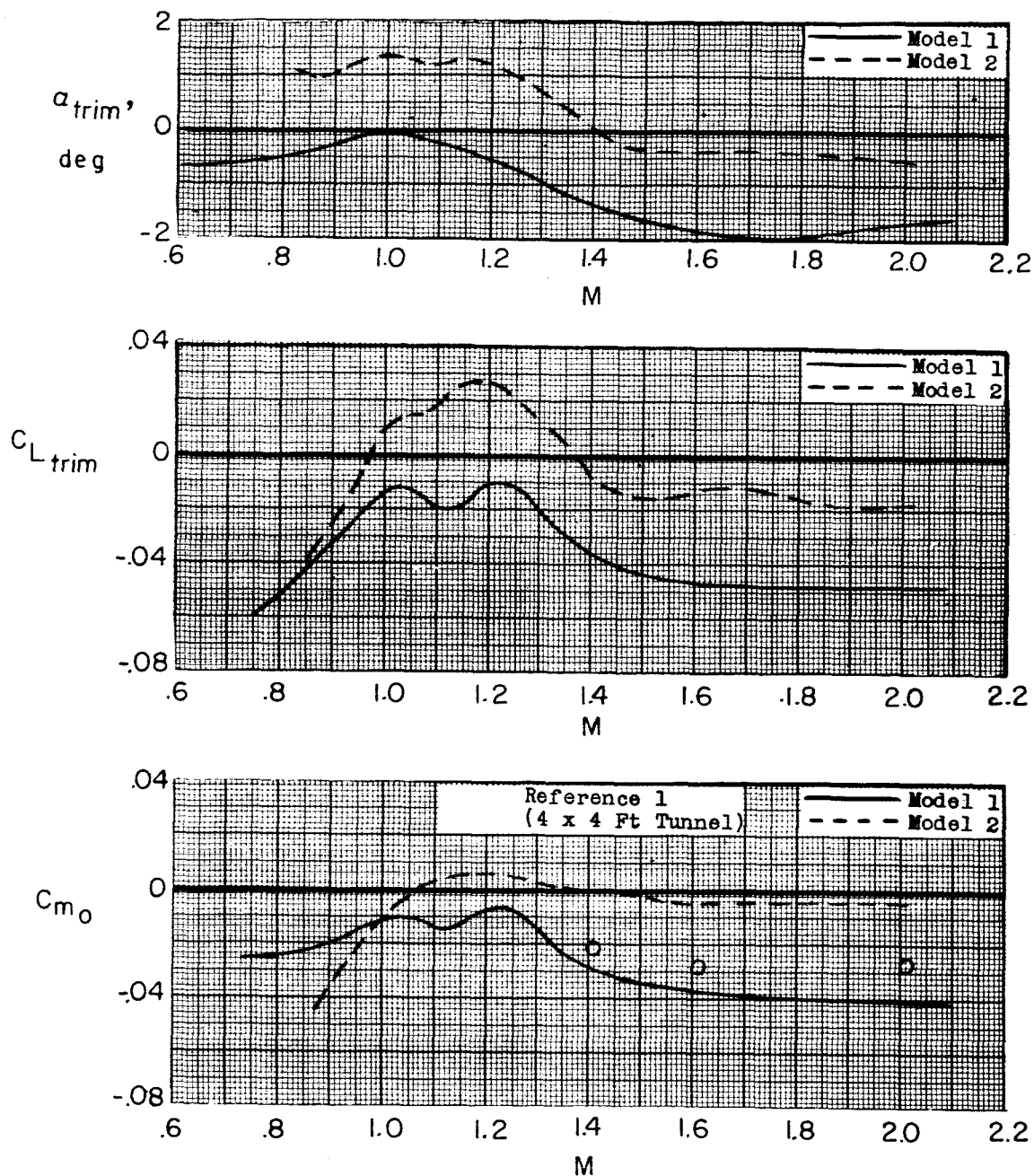
Figure 10.- Variation of trim characteristics and pitching-moment coefficient at zero lift with Mach number. Center of gravity located at 0.45c̄ ahead of the leading edge of c̄; elevons at zero deflection.
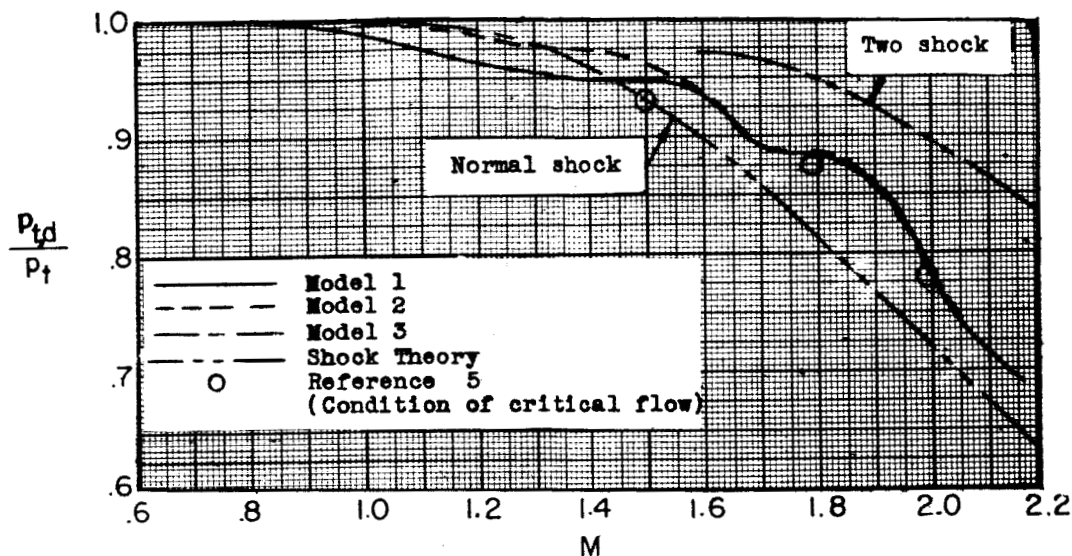
(a) Total-pressure recovery.
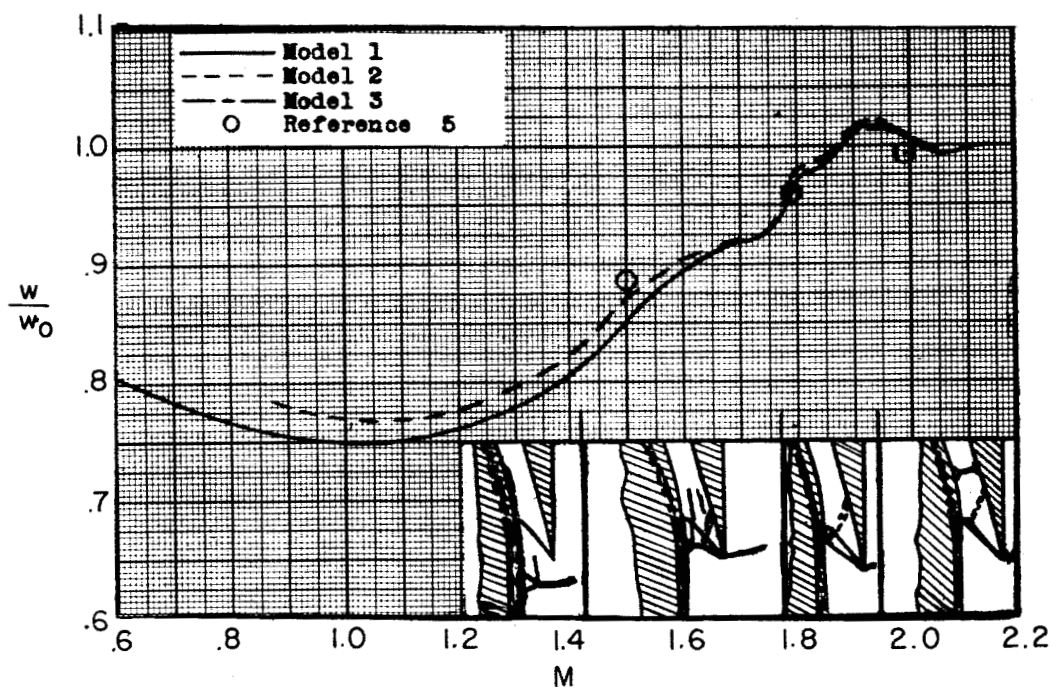
(b) Mass-flow ratio.

Figure 11.- Characteristics of duct at $\alpha = 0^O$.
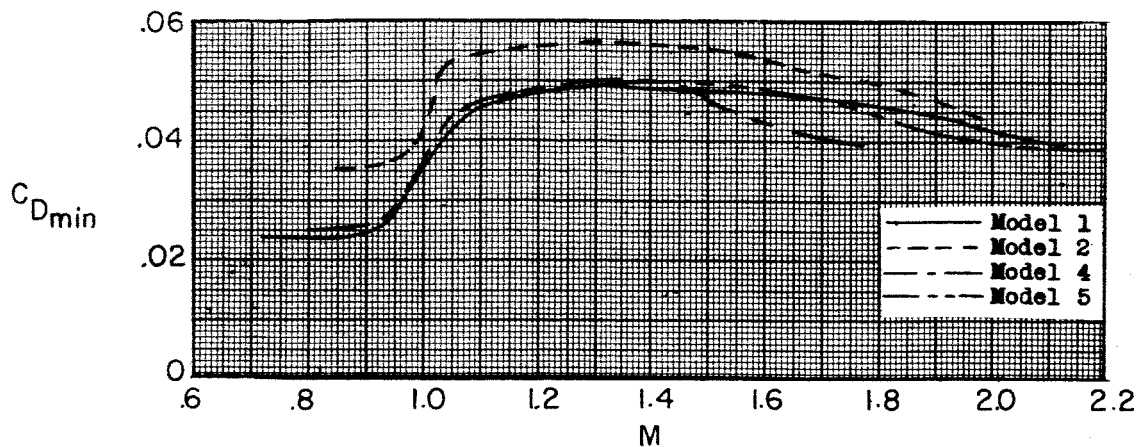
(a) Total measure.
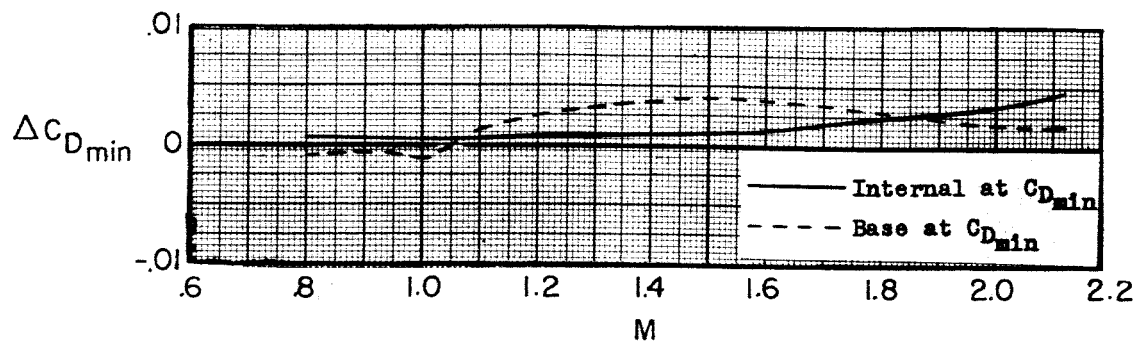
(b) Internal and base increments.
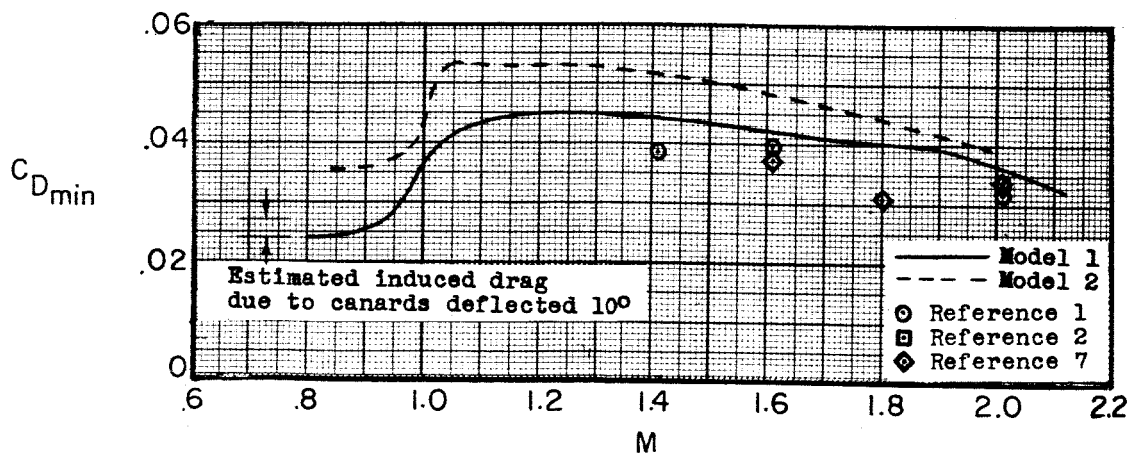
(c) External.

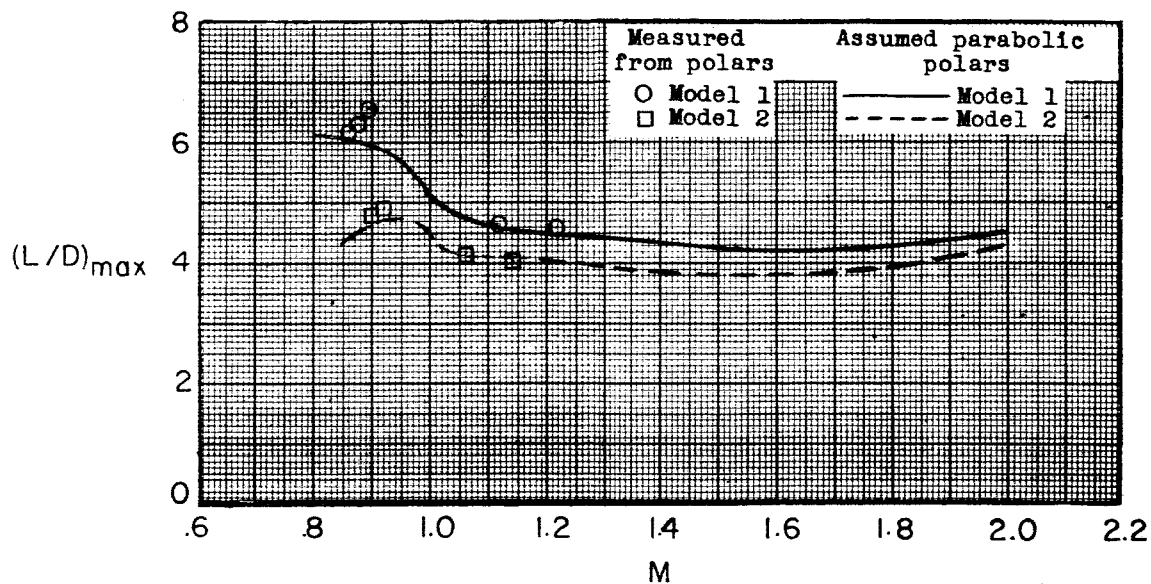Figure 12.- Variation of minimum-drag characteristics with Mach number.
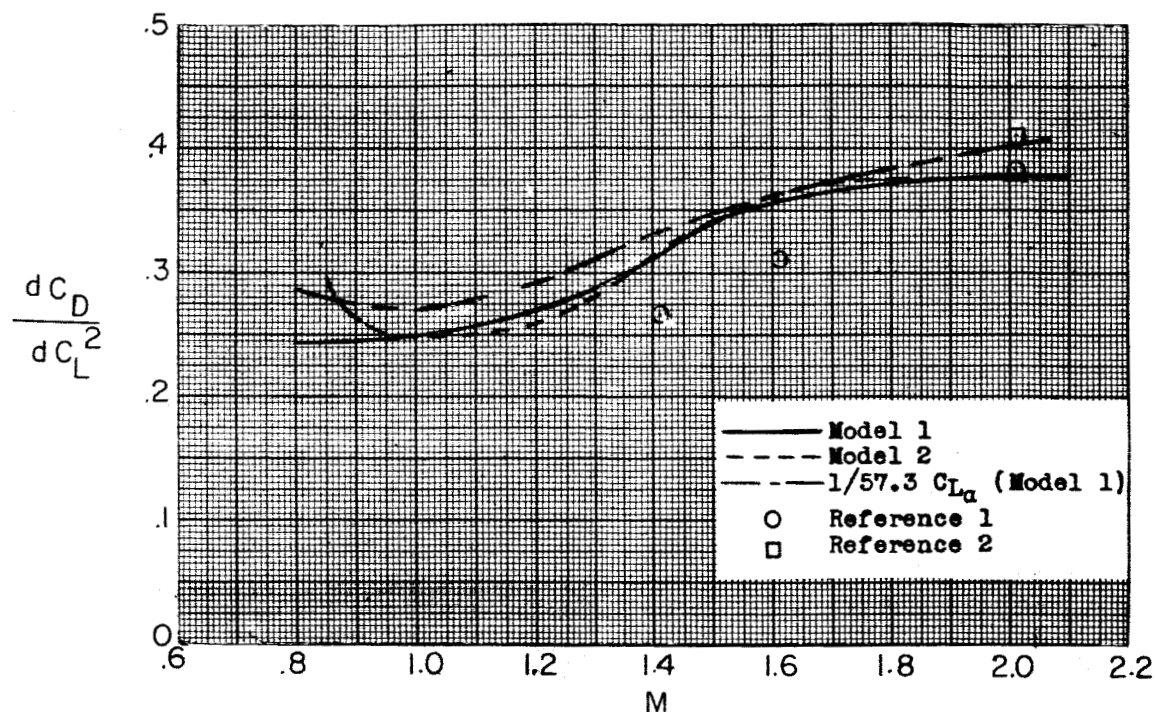
(a) Drag due to lift.
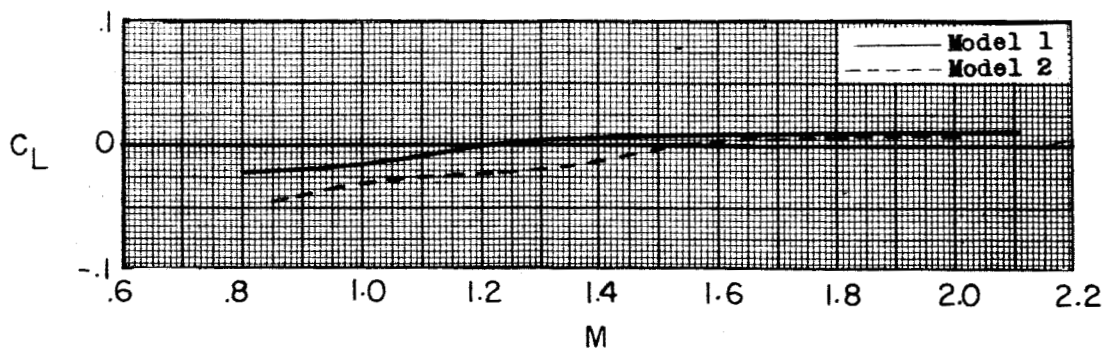
(b) Lift coefficient at minimum drag.

Figure 13.- Lift-drag relations. Zero elevon deflection.
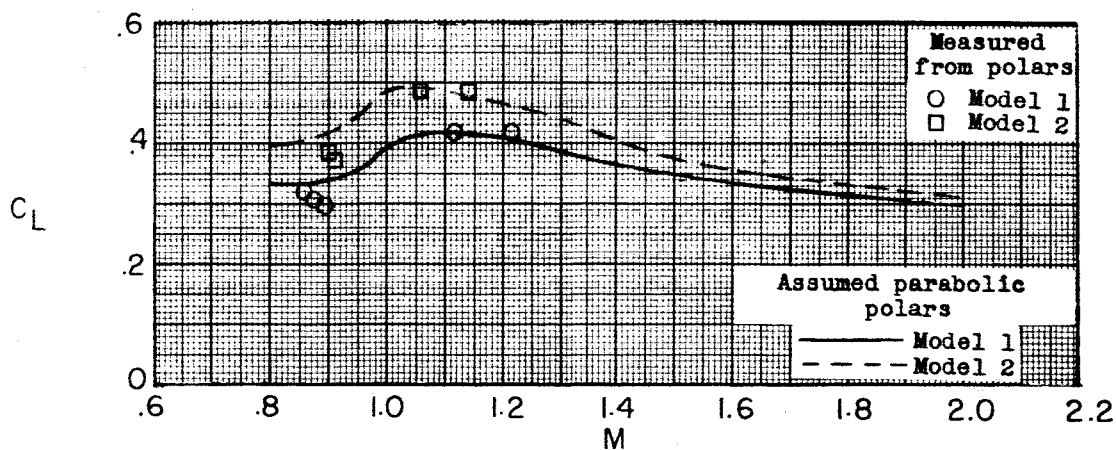
(c) Maximum lift-drag ratio.

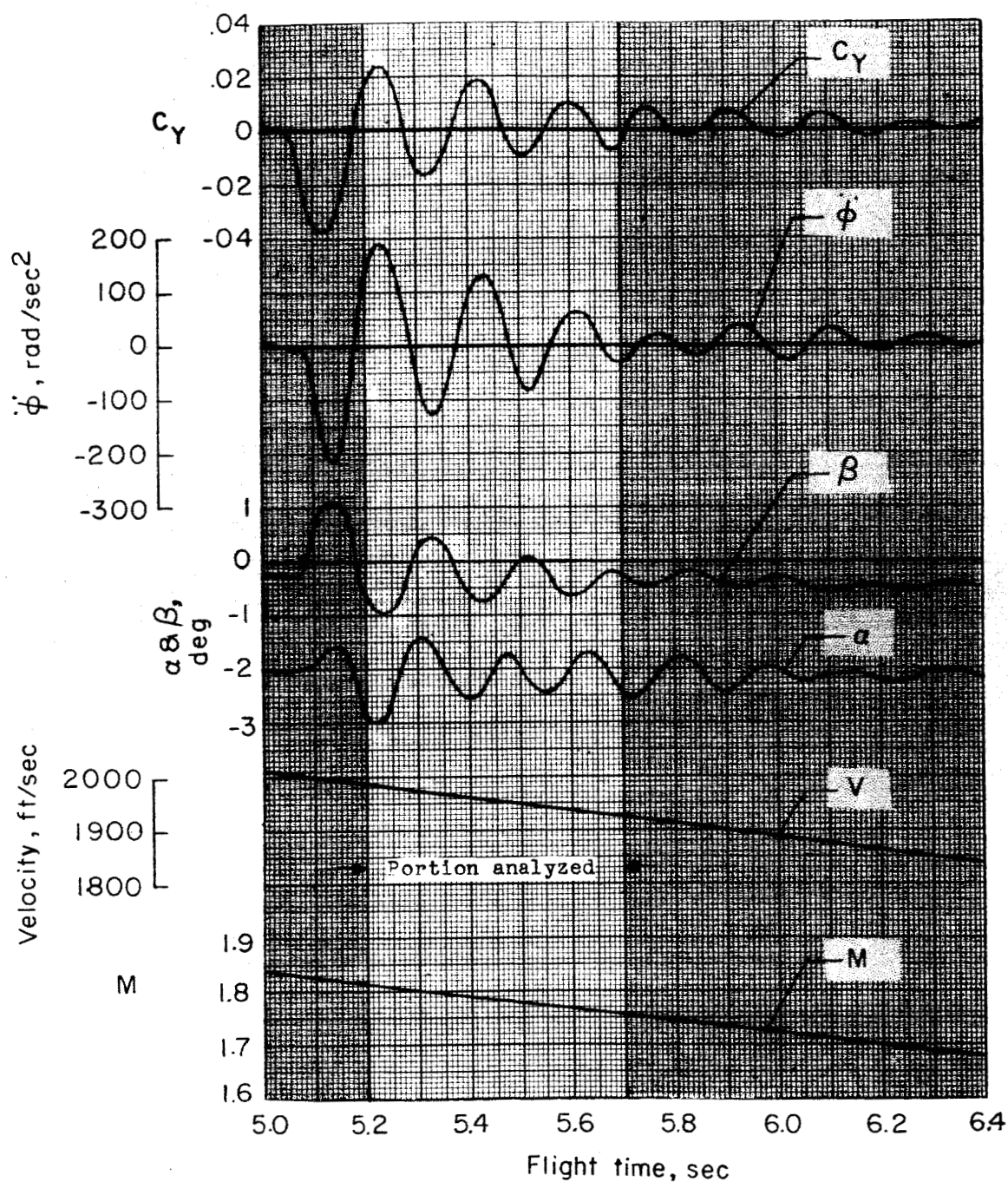(d) Lift coefficient for $(L/D)_{max}$.

Figure 13.- Concluded.

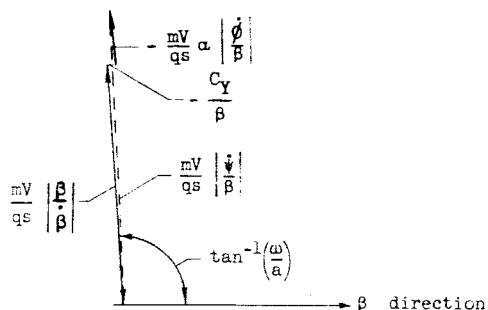Figure 14.- Time histories used in vector analysis of model 3.

Assume weight vector = 0

Solve for $\left|\dfrac{\dot{\psi}}{\beta}\right|$ and direction of $\dot{\psi}$ using

$$C_{Y_\beta} = -1.63$$

$$\alpha = -0.0379$$

$$a = 2.48$$

$$\omega = 36.3$$

Vector	Amplitude	Phase from β, deg
$\dfrac{mV}{qs}\left\|\dfrac{\dot{\beta}}{\beta}\right\|$	36.4	93.9
$\left\|\dfrac{C_Y}{\beta}\right\|$	1.63	0
$\left\|\dfrac{\ddot{\phi}}{\beta}\right\|$	12800.	190.0
$\left\|\dfrac{\dot{\phi}}{\beta}\right\|$	352.	96.1
$\dfrac{mV}{qs}\,\alpha\left\|\dfrac{\dot{\phi}}{\beta}\right\|$	12.0	96.1
$\dfrac{mV}{qs}\left\|\dfrac{\dot{\psi}}{\beta}\right\|$	*44.6	*273.1
$\left\|\dfrac{\dot{\psi}}{\beta}\right\|$	*49.6	*273.1
$\left\|\dfrac{\ddot{\psi}}{\beta}\right\|$	*1809.	*7.0

*Solutions of vector polygon.

$$\frac{mV}{qs}\left|\frac{\dot{\beta}}{\beta}\right| + \frac{mV}{qs}\left|\frac{\dot{\psi}}{\beta}\right| - \frac{mV}{qs}\,\alpha\left|\frac{\dot{\phi}}{\beta}\right| - \left|\frac{C_Y}{\beta}\right| = 0$$

(a) Solution of side-force equation.

Figure 15.- Vector diagrams with corresponding equations of motion for model 3 at M = 1.8. Coefficients in radian measure.
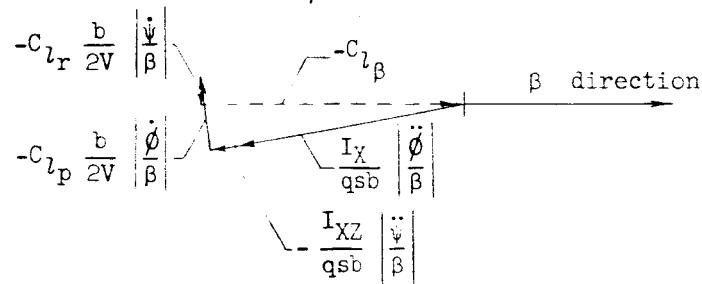
Assume value for C_{l_p}:

$$C_{l_p} = -0.404$$

Solve for C_{l_r} and C_{l_β}:

$$C_{l_r} = -1.13$$

$$C_{l_\beta} = -0.308$$

Vector	Amplitude	Phase from β, deg
$\dfrac{I_X}{qsb} \left\| \dfrac{\ddot{\phi}}{\beta} \right\|$	0.276	190.0
$\dfrac{I_{XZ}}{qsb} \left\| \dfrac{\ddot{\psi}}{\beta} \right\|$	.0298	187.0
$C_{l_p} \dfrac{b}{2V} \left\| \dfrac{\dot{\phi}}{\beta} \right\|$	.0855	96.1
$C_{l_r} \dfrac{b}{2V} \left\| \dfrac{\dot{\psi}}{\beta} \right\|$	*.0338	273.1
C_{l_β}	*.308	0

*Solution of vector polygon.

$$\frac{I_X}{qsb} \left| \frac{\ddot{\phi}}{\beta} \right| - \frac{I_{XZ}}{qsb} \left| \frac{\ddot{\psi}}{\beta} \right| - C_{l_r} \frac{b}{2V} \left| \frac{\dot{\psi}}{\beta} \right| - C_{l_p} \frac{b}{2V} \left| \frac{\dot{\phi}}{\beta} \right| - C_{l_\beta} = 0$$

(b) Solution of rolling-moment equation.

Figure 15.- Continued.

Assumed values of C_{n_p} and solve for respective values of C_{n_β} and $\left(C_{n_r} - C_{n_{\dot\beta}}\right)$:

$C_{n_p} = -0.1$ $\qquad$ $C_{n_p} = 0$ $\qquad$ $C_{n_p} = +0.1$
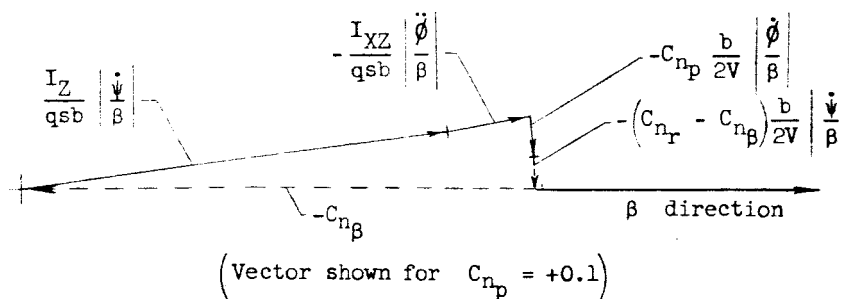
$C_{n_r} - C_{n_{\dot\beta}} = -4.95$ $\qquad$ $C_{n_r} - C_{n_{\dot\beta}} = -5.65$ $\qquad$ $C_{n_r} - C_{n_{\dot\beta}} = -6.36$

$C_{n_\beta} = 1.300$ $\qquad$ $C_{n_\beta} = 1.301$ $\qquad$ $C_{n_\beta} = 1.302$

$\left(\text{Vector shown for } C_{n_p} = +0.1\right)$

Vector	Amplitude			Phase from β, deg		
$\dfrac{I_Z}{qsb}\left\|\dfrac{\ddot\psi}{\beta}\right\|$	1.093			7.0		
$\dfrac{I_{XZ}}{qsb}\left\|\dfrac{\ddot\phi}{\beta}\right\|$	0.211			10.0		
Assumed C_{n_p}	+0.1	0	-0.1	+0.1	0	-0.1
$C_{n_p}\dfrac{b}{2V}\left\|\dfrac{\dot\phi}{\beta}\right\|$	0.0212	0	0.212	276.1	0	96.1
$\left(C_{n_r} - C_{n_{\dot\beta}}\right)\dfrac{b}{2V}\left\|\dfrac{\dot\psi}{\beta}\right\|$	*0.148	*0.170	*0.190	*273.1	*273.1	*273.1
C_{n_β}	*1.302	*1.301	*1.300	180	180	180

*Solution of vector polygon.

$$\frac{I_Z}{qsb}\left|\frac{\ddot\psi}{\beta}\right| - \frac{I_{XZ}}{qsb}\left|\frac{\ddot\phi}{\beta}\right| - C_{n_p}\frac{b}{2V}\left|\frac{\dot\phi}{\beta}\right| - \left(C_{n_r} - C_{n_{\dot\beta}}\right)\frac{b}{2V}\left|\frac{\dot\psi}{\beta}\right| - C_{n_\beta} = 0$$

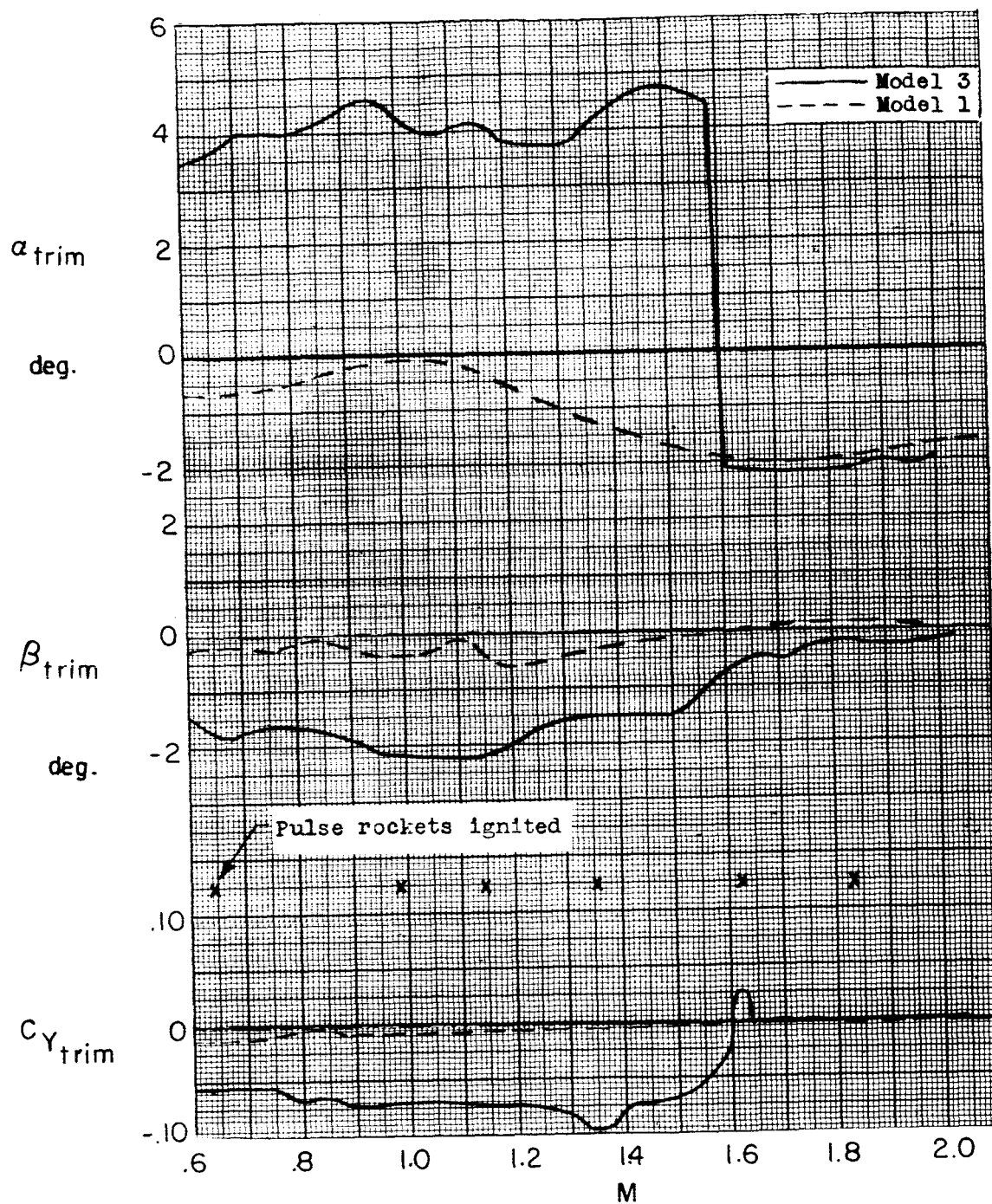(c) Solution of yawing-moment equation.

Figure 15.- Concluded.

Figure 16.- Trim characteristics of model 3 as compared with model 1.

$$\omega_\theta^2 = \frac{-C_{m_\alpha} q Sc}{I_y \dot\phi^2} \qquad \omega_\phi^2 = \frac{C_{n_\beta} q Sb}{I_z \dot\phi^2}$$

For M = 1.6

$$\omega_\theta^2 = \left(\frac{30.8}{\dot\phi}\right)^2 \qquad \omega_\psi^2 = \left(\frac{38.6}{\dot\phi}\right)^2$$
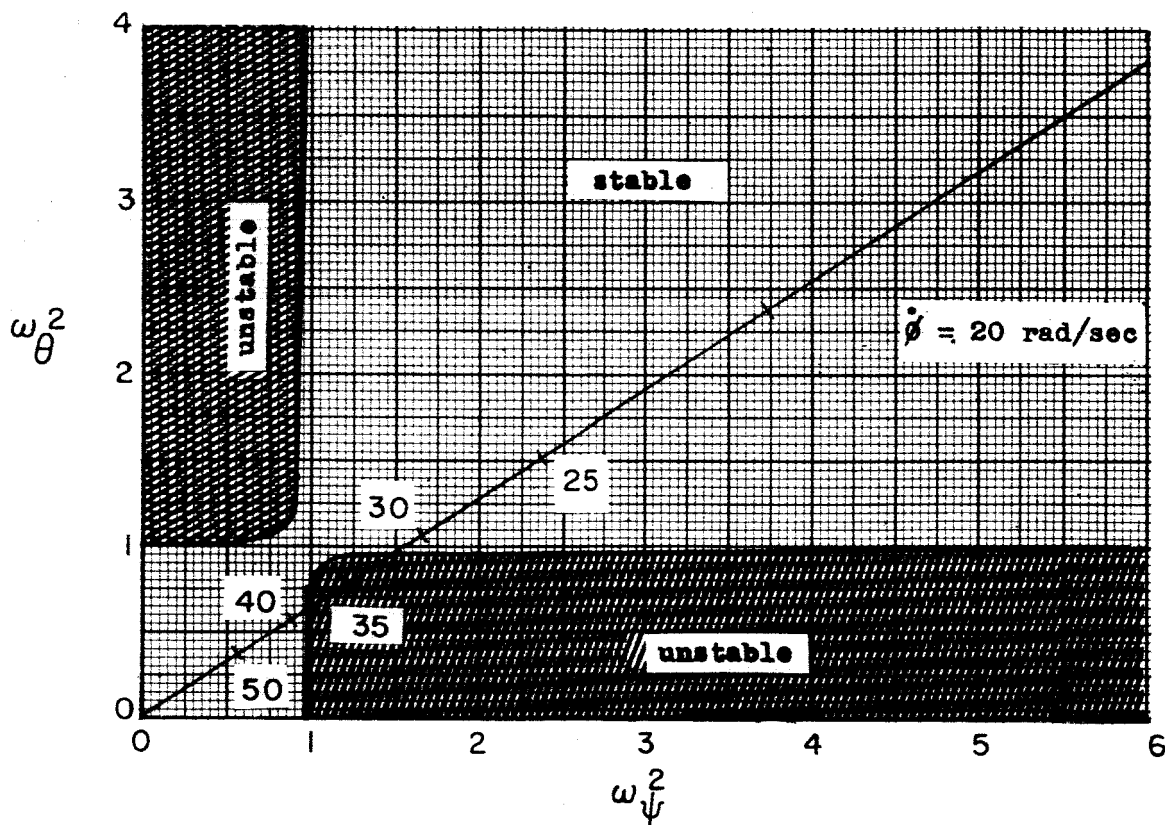
$$\zeta_\theta = .055 \qquad \zeta_\psi = .066$$

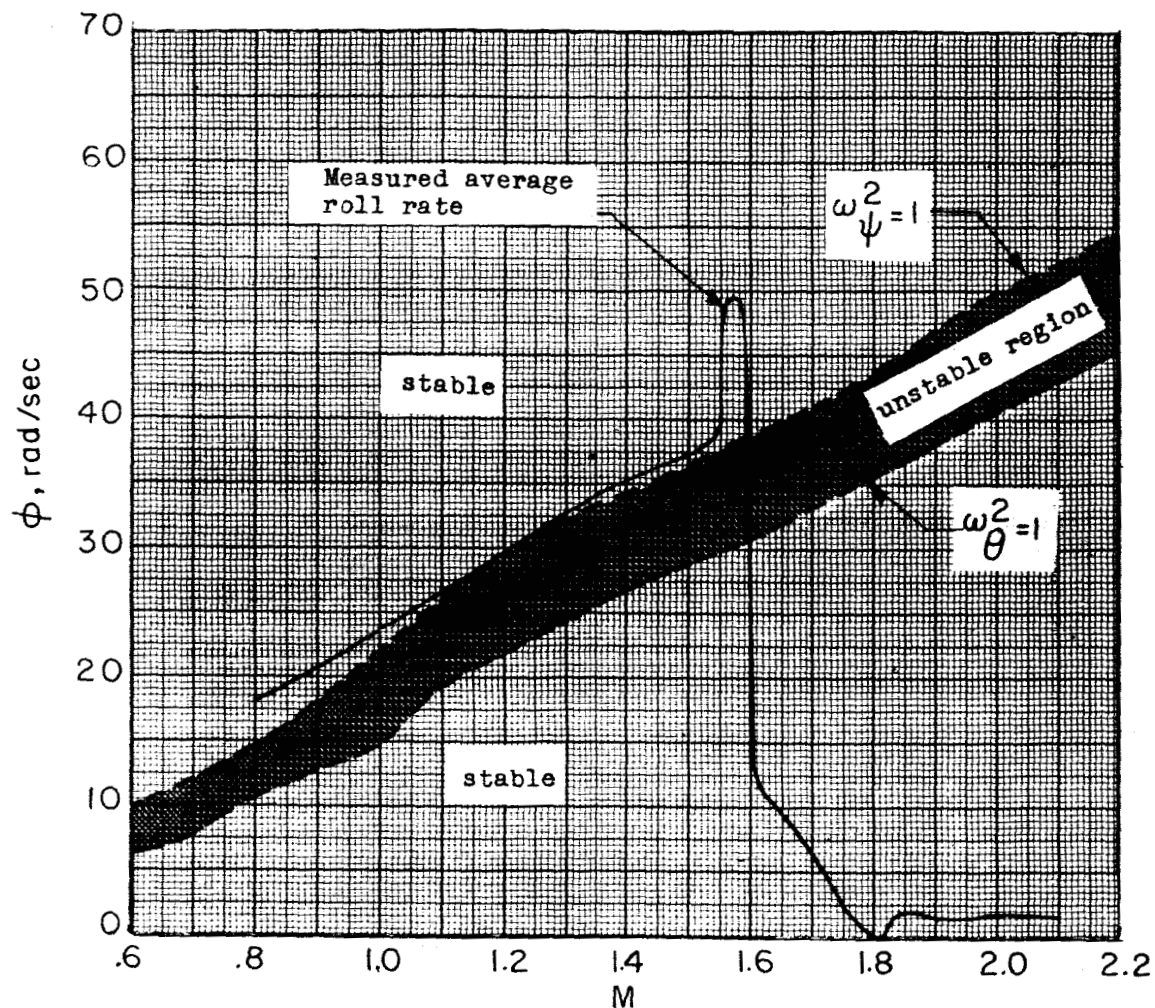Figure 17.- Divergence boundaries which include damping and roll rates of model 3 at M = 1.6.

Figure 18.- Rolling velocity of model 3, shown with estimates of rolling velocities required for resonance in pitch and yaw $\left(\omega_\theta{}^2 = \omega_\psi{}^2 = 1\right)$. No damping was included in the stability boundaries.

DECLASSIFIED

CONFIDENTIAL

SUMMARY OF FLIGHT DATA OBTAINED

FROM 0.12-SCALE ROCKET-POWERED MODELS OF THE

CHANCE VOUGHT REGULUS II MISSILE*

TED NO. NACA AD 398

By Andrew R. Wineman

ABSTRACT

Five models were flight tested at Mach numbers from 0.8 to 2.1 to determine the longitudinal static and dynamic stability, lateral static and dynamic stability, overall duct performance, and drag characteristics of three different configurations. Longitudinal trim problems were alleviated through the use of canard trimmers at the cost of minimum drag. Duct recoveries were good but spillage influenced the stability and drag at some Mach numbers. Lateral data were obtained only at a Mach number of 1.8 for a model with an oversized vertical tail. High roll rates with associated coupled motions between pitch and yaw were experienced and qualitatively analyzed for a lateral-stability model at Mach numbers from 0.8 to 1.8.

INDEX HEADINGS

---

*Title, Unclassified.

SUMMARY OF FLIGHT DATA OBTAINED

FROM 0.12-SCALE ROCKET-POWERED MODELS OF THE

CHANCE VOUGHT REGULUS II MISSILE

TED NO. NACA AD 398

Andrew R. Wineman

Andrew R. Wineman

Approved: *Joseph A. Shortal*
                      Joseph A. Shortal
         Chief of Pilotless Aircraft Research Division
                Langley Aeronautical Laboratory

bcd
(7/29/58)